

# Local Energy Decomposition of Open-Shell Molecular Systems in the Domain-Based Local Pair Natural Orbital Coupled Cluster Framework

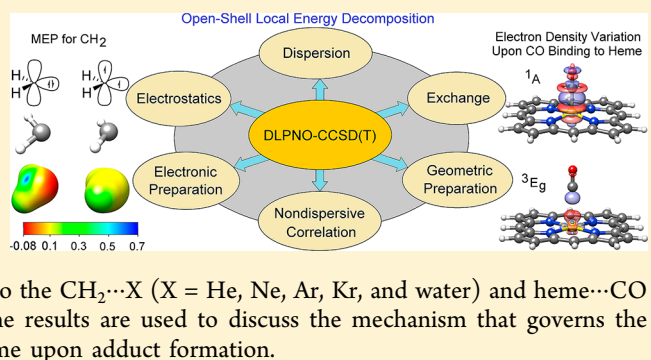
Ahmet Altun,<sup>†</sup> Masaaki Saitow,<sup>‡</sup> Frank Neese,<sup>\*,†</sup> and Giovanni Bistoni<sup>\*,†</sup>

<sup>†</sup>Max-Planck-Institut für Kohlenforschung, Kaiser-Wilhelm-Platz 1, D-45470 Mülheim an der Ruhr, Germany

<sup>‡</sup>Department of Chemistry, Graduate School of Science, Nagoya University, 1-5 Chikusa-ku, 464-8602 Nagoya, Japan

## Supporting Information

**ABSTRACT:** Local energy decomposition (LED) analysis decomposes the interaction energy between two fragments calculated at the domain-based local pair natural orbital CCSD(T) (DLPNO-CCSD(T)) level of theory into a series of chemically meaningful contributions and has found widespread applications in the study of noncovalent interactions. Herein, an extension of this scheme that allows for the analysis of interaction energies of open-shell molecular systems calculated at the UHF-DLPNO-CCSD(T) level is presented. The new scheme is illustrated through applications to the  $\text{CH}_2 \cdots \text{X}$  ( $\text{X} = \text{He}, \text{Ne}, \text{Ar}, \text{Kr},$  and water) and heme $\cdots\text{CO}$  interactions in the low-lying singlet and triplet spin states. The results are used to discuss the mechanism that governs the change in the singlet–triplet energy gap of methylene and heme upon adduct formation.



## 1. INTRODUCTION

Weak intermolecular interactions play a major role in virtually all areas of chemical research.<sup>1–6</sup> Perturbative and supermolecular approaches can be used to evaluate weak interaction energies between two or more fragments. Within a perturbative approach the Hamiltonian is partitioned into contributions of noninteracting fragment terms plus a series of perturbing potentials representing the interaction between the fragments. The most popular approach of this type is the symmetry-adapted perturbation theory (SAPT), which also provides a decomposition of the interaction energy into a series of physically meaningful contributions, including electrostatics, induction, London dispersion, and exchange-repulsion terms.<sup>7</sup> Although these interaction energy components have no unique definition, their quantification has been instrumental for the rationalization of the underlying mechanism that gives rise to the interaction.<sup>8</sup>

Within a supermolecular approach, the interaction energy is computed as the difference between the total energy of the adduct and the energy of the separated monomers. The decomposition of the resulting interaction energy into physical terms is then obtained via energy decomposition analysis (EDA) schemes, which are mainly based on a seminal work of Morokuma.<sup>9</sup> In these schemes the interaction energy is typically partitioned into electrostatics, charge transfer and/or polarization, and Pauli repulsion (also called exchange-repulsion) terms.<sup>10–14</sup>

The large majority of EDA schemes applied in mainstream computational chemistry relies on density functional theory (DFT) for the calculation of interaction energies. Hence, the

range of applicability of such schemes is limited by the accuracy of the chosen functional. This is especially limiting in the context of noncovalent interactions, as DFT does not properly describe London dispersion. Although several strategies have been suggested<sup>15–19</sup> in order to practically deal with this shortcoming, a quantitative understanding of weak interactions typically requires the use of highly correlated wave function-based ab initio methods in conjunction with large basis sets.<sup>8,20–23</sup>

In particular, the coupled-cluster method with single, double, and perturbative treatment of triple excitations, i.e., CCSD(T),<sup>22,24</sup> has proven its reliability in a wide range of contexts and typically allows one to compute relative energies with chemical accuracy (defined here as 1 kcal/mol). Unfortunately, the computational cost of CCSD(T) increases as the seventh power of the molecular size. Hence, the calculation of CCSD(T) energies is only possible for benchmark studies involving relatively small systems. To overcome this limitation, the domain-based local pair natural orbital CCSD(T) method, i.e., DLPNO-CCSD(T), was developed.<sup>25–34</sup> This technique typically retains the accuracy and reliability of CCSD(T), as shown on many benchmark data sets,<sup>34–37</sup> while allowing at the same time for the calculation of single-point energies for systems with thousands of basis functions.

In order to aid in the interpretation of DLPNO-CCSD(T) results, we recently introduced an EDA approach called local

Received: November 10, 2018

Published: January 31, 2019

energy decomposition (LED).<sup>38</sup> In this scheme, the interaction energy between two or more fragments is calculated at the DLPNO-CCSD(T) level and is then decomposed into a repulsive intramolecular energy term called electronic preparation, plus a series of intermolecular energy terms such as electrostatic, quantum mechanical exchange, and London dispersion interactions.<sup>38</sup> This scheme has been already applied in the context of H-bond interactions,<sup>38,39</sup> frustrated Lewis pairs,<sup>40</sup> agostic interactions,<sup>41</sup> and the interactions in dipnictenes.<sup>42</sup> Quantitative comparisons of the terms of LED and SAPT have been also reported.<sup>38,39</sup>

Herein, we present an extension of the LED scheme to open-shell systems in the framework of the DLPNO-CCSD(T) method. The present developments were made accessible through the recent ORCA 4.1 program release.<sup>43,44</sup> This opens an unprecedented opportunity for understanding and thus controlling a wide range of chemical and biological processes, especially in view of the limited number of previously developed EDA and SAPT approaches for open-shell molecular systems.<sup>45–52</sup> The new scheme is used to investigate the mechanism that governs the change in the singlet–triplet energy gap ( $E_{S-T}$ ) of carbenes upon their noncovalent interactions with various chemical species and of heme upon CO binding. The systems studied are as shown in Figure 1.

Carbenes are highly reactive neutral divalent molecules that exist in triplet and singlet spin states.<sup>53–62</sup> The singlet and triplet states of carbenes yield different reaction products. For

example, the simplest carbene  $\text{CH}_2$  (methylene), being one of the most reactive molecules, undergoes stereospecific reactions in the singlet state and stereoselective reactions in the triplet state.<sup>55–62</sup> Although many carbenes have a triplet ground state in the gas phase, the singlet state is typically stabilized significantly in several solvents, causing an equilibrium between the two spin states or even leading to a singlet ground state.<sup>55–62</sup>

Herein, the presently introduced open-shell variant of the DLPNO-CCSD(T)/LED scheme is applied to a series of prototypical molecular systems (Figure 1) of the type  $\text{CH}_2 \cdots \text{X}$ , in which methylene (in both its singlet  $^1\text{CH}_2$  and its triplet  $^3\text{CH}_2$  spin states) interacts through noncovalent interactions either with water or with rare gases (Rg = He, Ne, Ar, and Kr). The variation in the  $E_{S-T}$  of methylene upon adduct formation is discussed in terms of the  $^1\text{CH}_2 \cdots \text{X}$  and  $^3\text{CH}_2 \cdots \text{X}$  interaction energy components extracted from the LED scheme.

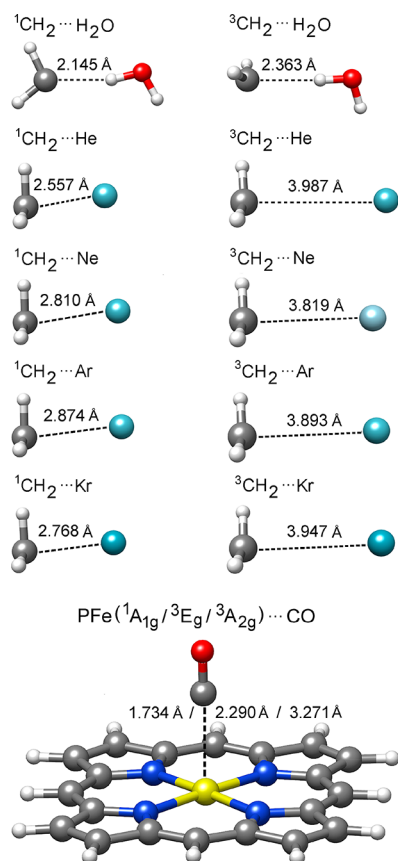
The other illustrative case study discussed here involves heme, which is an iron-coordinated porphyrin (P) derivative that is essential for the function of all aerobic cells.<sup>63</sup> It serves as a chromophore for many proteins including hemoglobin, myoglobin, and cytochromes, and thus regulates diverse biological functions.<sup>64,65</sup>

Heme owes its functional diversity in the protein matrix to its differing side chain environments, bound axial ligands and their environments, coordination number, and oxidation and spin states of the iron center.<sup>65</sup> In particular, the binding and dissociation reactions of CO to the ferrous heme in the protein matrix have significant impacts on its role in respiration and regulation processes.<sup>66</sup> Experimentally, it is known that ferrous iron-coordinated porphyrin (PFe, also denoted hereafter as free heme) derivatives and their CO-bound PFe $\cdots$ CO analogs have triplet and singlet ground states, respectively.<sup>67–70</sup> Thus, the CO binding reverses the spin-state ordering of heme derivatives. However, the chemical mechanism behind this experimental observation is not clear.

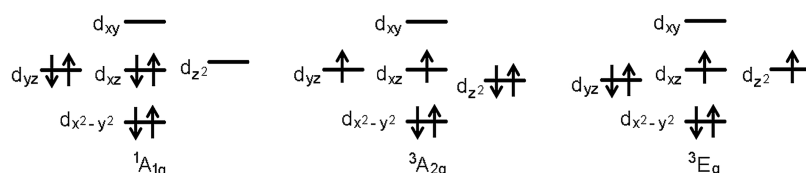
Herein, the LED scheme is used to provide a first insight into the factors contributing to the stabilization of the lowest-lying singlet state ( $^1\text{A}_1\text{g}$ ) and two close-lying lowest-energy triplets ( $^3\text{E}_\text{g}$  and  $^3\text{A}_2\text{g}$ ) of PFe (see Scheme 1) upon CO binding, i.e., the PFe( $^1\text{A}_1\text{g}/^3\text{E}_\text{g}/^3\text{A}_2\text{g}$ ) $\cdots$ CO interactions. As seen in Scheme 1, the  $^1\text{A}_1\text{g}$  singlet has an electronic configuration of  $(d_{x^2-y^2})^2(d_{yz})^2(d_{xz})^2(d_z)^0(d_{xy})^0$  while the  $^3\text{A}_2\text{g}$  and  $^3\text{E}_\text{g}$  triplets have the  $(d_{x^2-y^2})^2(d_z)^2(d_{yz})^1(d_{xz})^1(d_{xy})^0$  and  $(d_{x^2-y^2})^2(d_{yz})^2(d_{xz})^1(d_z)^1(d_{xy})^0$  configurations, respectively.

As a prototype case study, we focus on the bare porphyrin that has no peripheral or other axial substituents (see Figure 1). It should be emphasized here that spin-state ordering of heme species is dependent on such substituents as well as on their surrounding media.<sup>71</sup> For example, if a single imidazole ligand is bound to the free heme rather than CO then the quintet state becomes the ground state both in the solid phase and in protein matrices.<sup>72</sup> A thorough analysis of the role of different substituents and surrounding media on the singlet–triplet energy gap of heme species would require an extensive systematic study, which is beyond the scope of this study.

The paper is organized as follows. In section 2 the theory of the open-shell LED scheme is given, while computational details are reported in section 3. In section 4, the  $E_{S-T}$  singlet–triplet energy gap of methylene, heme, and their investigated adducts is reported at the DLPNO-CCSD(T) level. Then in the framework of the presently introduced open-shell DLPNO-CCSD(T)/LED method, the variations in  $E_{S-T}$  of methylene



**Figure 1.** Investigated  $\text{CH}_2 \cdots \text{X}$  and PFe $\cdots$ CO adducts and the associated equilibrium intermolecular distances obtained at the DLPNO-CCSD(T)/TightPNO/aug-cc-pVTZ and B3LYP-D3/def2-TZVP levels, respectively.

Scheme 1. Simple Schematic Representation of the Singlet and Low-Lying Triplet Electronic Configurations of PFe and PFe...CO<sup>a</sup>

<sup>a</sup>One of the degenerate pair of  ${}^3E_g$  configurations is shown. The other configuration is clearly  $(d_{x^2-y^2})^2(d_{yz})^1(d_{xz})^1(d_z^2)^1(d_{xy})^0$ .

and heme upon the formation of the adducts are discussed in terms of the corresponding LED interaction energy components for the low-lying singlet and triplet states. The dependence of the results on the various technical aspects of the calculations is discussed in the [Supporting Information](#) (Tables S2–S13). The distance dependence of the open-shell LED terms is discussed in [section 4](#) for the PFe-( ${}^1A_{1g}/{}^3A_{2g}/{}^3E_g$ )...CO interaction and given in [Figure S1](#) for the CH<sub>2</sub>...H<sub>2</sub>O interaction. The last section of the paper is devoted to discussion of the results and concluding remarks of the study.

## 2. THEORY

**2.1. Theoretical Background.** The theory and implementation of the DLPNO-CCSD(T) method in both its closed-shell and its open-shell variants have been described in detail in a series of recent publications.<sup>25–34,38,73,74</sup> We thus only recall here the energy expression for the open-shell DLPNO-CCSD(T) method, which is decomposed in the present variant of the LED scheme.

The total DLPNO-CCSD(T) energy can be expressed as a sum of reference and correlation energies  $E = E_{\text{ref}} + E_C$ . In the closed-shell variant of DLPNO-CCSD(T), the reference determinant is typically the Hartree–Fock (HF) determinant, and hence,  $E_{\text{ref}}$  corresponds to the HF energy. In the open-shell variant,  $E_{\text{ref}}$  is the energy of a high-spin open-shell single determinantal function, consisting of a single set of molecular orbitals. The energy of such a determinant can be expressed as

$$E_{\text{ref}} = \sum_{A>B} \frac{Z_A Z_B}{|\mathbf{R}_A - \mathbf{R}_B|} + \sum_i \frac{n_i}{2} \langle i | -\nabla_i^2 | i \rangle + \sum_{i,A} n_i \left\langle i \left| \frac{Z_A}{|\mathbf{r}_i - \mathbf{R}_A|} \right| i \right\rangle + \sum_{i \geq j} [n_i n_j \cdot (ilij) - (n_{i,\alpha} n_{j,\alpha} + n_{i,\beta} n_{j,\beta}) \cdot (ijlj)] \quad (1)$$

where  $i$  and  $j$  are the occupied orbitals of the reference determinant,  $n_{i,\alpha}$  and  $n_{i,\beta}$  denote the occupation numbers (1 or 0) for  $\alpha$  and  $\beta$  electrons, respectively,  $n_i = n_{i,\alpha} + n_{i,\beta}$ ;  $(ilij)$  and  $(ijlj)$  are two electrons integrals in Mulliken notation, and  $Z_A$  ( $Z_B$ ) is the nuclear charge of atom  $A$  ( $B$ ) at position  $\mathbf{R}_A$  ( $\mathbf{R}_B$ ).

The DLPNO-CCSD(T) correlation energy can be written essentially as a sum of electron-pair correlation energy ( $\varepsilon_{ij}$  where  $i$  and  $j$  denote the localized orbitals) contributions plus the perturbative triples correction ( $E_{C-(T)}$ ). Local second-order many-body perturbation theory is used to divide the  $\varepsilon_{ij}$  terms into “weak pairs”, with an expected negligible contribution to the correlation energy, and “strong pairs”. The contribution coming from the weak pairs is kept at the second-order level, whereas the strong pairs are treated at the coupled cluster level. Hence, the overall correlation energy reads

$$E_C = E_{C\text{-SP}} + E_{C\text{-WP}} + E_{C\text{-(T)}} \quad (2)$$

where  $E_{C\text{-SP}}$  denotes the energy contribution from the strong pairs,  $E_{C\text{-WP}}$  is the correlation contribution from the weak pairs, and the last term is associated with the perturbative triples correction  $E_{C\text{-(T)}}$ .

The dominant strong pair contribution reads

$$E_{C\text{-SP}} = \sum_{i,a_i} F_{i,a_i} t_{a_i}^i + \sum_{\bar{i},\bar{a}_i} F_{\bar{i},\bar{a}_i} t_{\bar{a}_i}^{\bar{i}} + \sum_{i>j} \varepsilon_{ij} + \sum_{\bar{i}>\bar{j}} \varepsilon_{\bar{i}\bar{j}} + \sum_{i\bar{j}} \varepsilon_{i\bar{j}} \quad (3)$$

where the indices with an overbar denote  $\beta$  spin-orbitals and those without overbar are used for  $\alpha$  spin-orbitals. The first two terms represent the contribution from the single excitations ( $a_i$ , the singles PNOs;  $t_{a_i}^i$ , the singles amplitudes). These terms vanish if the Brillouin’s theorem is satisfied.<sup>73</sup> This is not generally the case when the quasi-restricted orbitals (QROs)<sup>75</sup> or restricted open-shell HF (ROHF) determinant is used, the former of which is the standard choice in open-shell DLPNO-CCSD(T) calculations.<sup>73</sup> The  $\varepsilon_{ij}$ ,  $\varepsilon_{\bar{i}\bar{j}}$  and  $\varepsilon_{i\bar{j}}$  terms denote  $\alpha$ – $\alpha$ ,  $\beta$ – $\beta$ , and  $\alpha$ – $\beta$  pair correlation energies, defined as

$$\varepsilon_{ij} = \frac{1}{2} \sum_{a_j b_j} [(i a_{ij} | j b_{ij}) - (i b_{ij} | j a_{ij})] \tau_{a_j b_j}^{ij} \quad (4)$$

$$\varepsilon_{\bar{i}\bar{j}} = \frac{1}{2} \sum_{\bar{a}_j \bar{b}_j} [(\bar{i} \bar{a}_{\bar{i}\bar{j}} | \bar{j} \bar{b}_{\bar{i}\bar{j}}) - (\bar{i} \bar{b}_{\bar{i}\bar{j}} | \bar{j} \bar{a}_{\bar{i}\bar{j}})] \tau_{\bar{a}_j \bar{b}_j}^{\bar{i}\bar{j}} \quad (5)$$

$$\varepsilon_{i\bar{j}} = \sum_{a_j \bar{b}_j} (i a_{i\bar{j}} | \bar{j} \bar{b}_{i\bar{j}}) \tau_{a_j \bar{b}_j}^{i\bar{j}} \quad (6)$$

where  $a_{ij}$  and  $b_{ij}$  are the PNOs belonging to the  $ij$  pair,  $(i a_{ij} | j b_{ij})$  are the two-electrons integrals,  $\tau_{a_j b_j}^{ij} = t_{a_j b_j}^{ij} + t_{a_j}^i t_{b_j}^j - t_{b_j}^j t_{a_j}^i$  and  $\tau_{\bar{a}_j \bar{b}_j}^{\bar{i}\bar{j}} = t_{\bar{a}_j \bar{b}_j}^{\bar{i}\bar{j}} + t_{\bar{a}_j}^{\bar{i}} t_{\bar{b}_j}^{\bar{j}} - t_{\bar{b}_j}^{\bar{j}} t_{\bar{a}_j}^{\bar{i}}$  are the cluster amplitudes in the PNO basis, and  $t_{a_j b_j}^{ij}$ ,  $t_{a_j}^i$ ,  $t_{b_j}^j$  are the doubles and singles amplitudes of the coupled cluster equations.

**2.2. Open-Shell Variant of the Local Energy Decomposition.** Within a supermolecular approach, the energy of a molecular adduct XY relative to the total energies of noninteracting fragments X and Y, i.e., the binding energy of the fragments ( $\Delta E$ ), can be written as

$$\Delta E = \Delta E_{\text{geo-prep}} + \Delta E_{\text{int}} \quad (7)$$

where  $\Delta E_{\text{geo-prep}}$  is the geometric preparation energy needed to distort the fragments X and Y from their structures at infinite separation to their in-adduct geometry.  $\Delta E_{\text{int}}$  is the interaction

energy between the fragments X and Y frozen in the geometry they have in the adduct XY, which is defined as

$$\Delta E_{\text{int}} = E^{\text{XY}} - E^{\text{X}} - E^{\text{Y}} \quad (8)$$

where  $E^{\text{XY}}$  is energy of the XY adduct while  $E^{\text{X}}$  ( $E^{\text{Y}}$ ) is the energy of the isolated X (Y) fragment frozen at the same geometry as that in the adduct.  $\Delta E_{\text{int}}$  can be decomposed into a reference contribution  $\Delta E_{\text{int}}^{\text{ref}}$  (i.e., the contribution to the interaction energy from the QRO determinant in the open shell case) and a correlation contribution  $\Delta E_{\text{int}}^{\text{C}}$

$$\begin{aligned} \Delta E_{\text{int}} &= (E_{\text{ref}}^{\text{XY}} - E_{\text{ref}}^{\text{X}} - E_{\text{ref}}^{\text{Y}}) + (E_{\text{C}}^{\text{XY}} - E_{\text{C}}^{\text{X}} - E_{\text{C}}^{\text{Y}}) \\ &= \Delta E_{\text{int}}^{\text{ref}} + \Delta E_{\text{int}}^{\text{C}} \end{aligned} \quad (9)$$

In the DLPNO-CCSD(T) framework, the orbitals of the reference determinant are initially localized. Hence, each orbital can be usually assigned to the fragment where it is dominantly localized. By exploiting the localization of the occupied orbitals, it is possible to regroup the terms of the reference energy of the XY adduct  $E_{\text{ref}}^{\text{XY}}$  (eq 1) into intra- and intermolecular contributions in exactly the same way as it was described for the closed-shell case<sup>38,40</sup>

$$E_{\text{ref}}^{\text{XY}} = E_{\text{ref}}^{\text{(X)}} + E_{\text{ref}}^{\text{(Y)}} + E_{\text{ref}}^{\text{(X,Y)}} \quad (10)$$

The intermolecular reference energy can be further partitioned into electrostatic ( $E_{\text{elstat}}^{\text{ref}}$ ) and exchange ( $E_{\text{exch}}^{\text{ref}}$ ) interactions. Accordingly, the  $\Delta E_{\text{int}}^{\text{ref}}$  term can be written as

$$\begin{aligned} \Delta E_{\text{int}}^{\text{ref}} &= (E_{\text{ref}}^{\text{(X)}} + E_{\text{ref}}^{\text{(Y)}} - E_{\text{ref}}^{\text{X}} - E_{\text{ref}}^{\text{Y}}) + E_{\text{elstat}}^{\text{ref}} + E_{\text{exch}}^{\text{ref}} \\ &= \Delta E_{\text{el-prep}}^{\text{ref}} + E_{\text{elstat}}^{\text{ref}} + E_{\text{exch}}^{\text{ref}} \end{aligned} \quad (11)$$

The electronic preparation energy  $\Delta E_{\text{el-prep}}^{\text{ref}}$  is positive and thus repulsive. It corresponds to the energy needed to bring the electronic structures of the isolated fragments into the one that is optimal for the interaction.  $E_{\text{elstat}}$  and  $E_{\text{exch}}$  are the electrostatic and exchange interactions between the interacting fragments, respectively (note that the “ref” superscript in these terms is omitted for the sake of simplicity from now on). It is worth noting here that the intermolecular exchange describes a stabilizing component of the interaction, lowering the repulsion between electrons of the same spin. Note that  $E_{\text{elstat}}$  incorporates the Coulomb interaction between the *distorted* electronic clouds of the fragments. Hence, it accounts for both *induced* and *permanent* electrostatics. We recently proposed an approach for disentangling these two contributions in  $E_{\text{elstat}}$  in the closed-shell case,<sup>76</sup> which is in principle also applicable to the open-shell case.

The correlation contribution to the interaction energy  $E_{\text{int}}^{\text{C}}$  can thus be expressed as a sum of three contributions

$$\begin{aligned} \Delta E_{\text{int}}^{\text{C}} &= (E_{\text{C-SP}}^{\text{XY}} - E_{\text{C-SP}}^{\text{X}} - E_{\text{C-SP}}^{\text{Y}}) + (E_{\text{C-WP}}^{\text{XY}} - E_{\text{C-WP}}^{\text{X}} - E_{\text{C-WP}}^{\text{Y}}) \\ &\quad + (E_{\text{C-(T)}}^{\text{XY}} - E_{\text{C-(T)}}^{\text{X}} - E_{\text{C-(T)}}^{\text{Y}}) \\ &= \Delta E_{\text{int}}^{\text{C-SP}} + \Delta E_{\text{int}}^{\text{C-WP}} + \Delta E_{\text{int}}^{\text{C-(T)}} \end{aligned} \quad (12)$$

where  $\Delta E_{\text{int}}^{\text{C-SP}}$ ,  $\Delta E_{\text{int}}^{\text{C-WP}}$ , and  $\Delta E_{\text{int}}^{\text{C-(T)}}$  are the strong pairs, weak pairs, and triples correction components of the correlation contribution to the interaction energy, respectively. The  $\Delta E_{\text{int}}^{\text{C-SP}}$ ,  $\Delta E_{\text{int}}^{\text{C-WP}}$ , and  $\Delta E_{\text{int}}^{\text{C-(T)}}$  terms can be further divided into electronic preparation and interfragment interaction energies based on the localization of the occupied orbitals, as already described previously.<sup>31</sup>

For the (typically) dominant  $\Delta E_{\text{int}}^{\text{C-SP}}$  contribution, a more sophisticated approach is used in order to provide a clear-cut

definition of London dispersion. The  $E_{\text{C-SP}}^{\text{XY}}$  term can be written as a sum of the contributions of single and double excitations according to eqs 3–6. By exploiting the localization of both the occupied and the virtual orbitals in the DLPNO-CCSD(T) framework,  $E_{\text{C-SP}}^{\text{XY}}$  can be divided into five different contributions

$$E_{\text{C-SP}}^{\text{XY}} = E_{\text{C-SP}}^{\text{(X)}} + E_{\text{C-SP}}^{\text{(Y)}} + E_{\text{C-SP}}^{\text{CT(X→Y)}} + E_{\text{C-SP}}^{\text{CT(X←Y)}} + E_{\text{C-SP}}^{\text{DISP(X,Y)}} \quad (13)$$

where each energy term contains contributions from the  $\alpha\alpha$ ,  $\beta\beta$ , and  $\alpha\beta$  excitations constituting the correlation energy, as given in eqs 4–6. The corresponding energy expressions of these terms are reported in the following. Note that the subscript  $ij$  in the PNOs is omitted for clarity and that the indices X and Y represent the fragment on which the orbital is dominantly localized. For the sake of simplicity, only contributions from the  $\alpha\alpha$  pairs (and singles excitations of  $\alpha$  spin-orbitals) are shown as an example

$$\begin{aligned} E_{\text{C-SP}}^{\text{(X)}}(\alpha\alpha) &= \frac{1}{2} \sum_{i_X > j_X} \sum_{a_X b_X} [(i_X a_X | j_X b_X) - (i_X b_X | j_X a_X)] \tau_{a_X b_X}^{i_X j_X} \\ &\quad + \sum_{i_X, a_X} F_{i_X, a_X} t_{a_X}^{i_X} \end{aligned} \quad (14)$$

$$\begin{aligned} E_{\text{C-SP}}^{\text{CT(X→Y)}}(\alpha\alpha) &= \frac{1}{2} \sum_{i_X > j_X} \sum_{a_X b_Y} [(i_X a_X | j_X b_Y) - (i_X b_Y | j_X a_X)] \tau_{a_X b_Y}^{i_X j_X} \\ &\quad + \frac{1}{2} \sum_{i_X > j_X} \sum_{a_Y b_Y} [(i_X a_Y | j_X b_Y) - (i_X b_Y | j_X a_Y)] \tau_{a_Y b_Y}^{i_X j_Y} \\ &\quad + \frac{1}{2} \sum_{i_X > j_Y} \sum_{a_Y b_Y} [(i_X a_Y | j_Y b_Y) - (i_X b_Y | j_Y a_Y)] \tau_{a_Y b_Y}^{i_X j_Y} \\ &\quad + \frac{1}{2} \sum_{i_Y > j_X} \sum_{a_Y b_Y} [(i_Y a_Y | j_X b_Y) - (i_Y b_Y | j_X a_Y)] \tau_{a_Y b_Y}^{i_Y j_X} \end{aligned} \quad (15)$$

$$\begin{aligned} E_{\text{C-SP}}^{\text{DISP(X,Y)}}(\alpha\alpha) &= P_{X \leftrightarrow Y} \left[ \sum_{i_X > j_Y} \sum_{a_X b_X} [(i_X a_X | j_Y b_X) - (i_X b_X | j_Y a_X)] \tau_{a_X b_X}^{i_X j_Y} \right. \\ &\quad \left. + \sum_{i_X > j_Y} \sum_{a_Y b_X} [(i_X a_Y | j_Y b_X) - (i_X b_X | j_Y a_Y)] \tau_{a_Y b_X}^{i_X j_Y} \right] \end{aligned} \quad (16)$$

The  $E_{\text{C-SP}}^{\text{(Y)}}$  and  $E_{\text{C-SP}}^{\text{CT(X←Y)}}$  terms can be obtained from eqs 14 and 15 by exchanging the X and Y labels in all terms. Note that the last term in  $E_{\text{C-SP}}^{\text{(X)}}$  denotes the contribution from the singles excitations, whose physical meaning will be discussed later in this section. The relevant pair excitation contributions constituting these terms are shown pictorially in Figure 2.

$E_{\text{C-SP}}^{\text{(X)}}$  and  $E_{\text{C-SP}}^{\text{(Y)}}$  describe the correlation contribution from excitations occurring within the same fragment (also called intrafragment correlation). The dynamic charge transfer (CT) terms  $E_{\text{C-SP}}^{\text{CT(X→Y)}}$  and  $E_{\text{C-SP}}^{\text{CT(X←Y)}}$  represent the correlation energy contributions that arise from instantaneous cation–anion pair formations. In contrast to the Coulombic interaction energy decaying with  $r^{-1}$ , they occur with a small probability decaying exponentially with distance. These terms are essential for correcting overpolarized electron densities at the reference level.  $E_{\text{C-SP}}^{\text{DISP(X,Y)}}$  describes the energy contribution associated with genuine and exchange dispersion (see Figure 2).

For the sake of simplicity, it may be useful to combine several terms. For example,  $\Delta E_{\text{el-prep}}^{\text{C-SP}}$  (i.e., the difference between the intrafragment contributions  $E_{\text{C-SP}}^{\text{(X/Y)}}$  and the strong

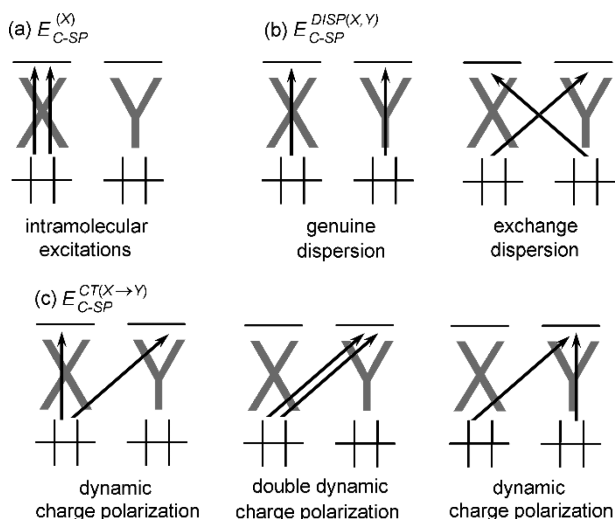


**Figure 2.** Schematic representation of strong pair excitations from occupied orbitals to virtual orbitals (PNOs) in the framework of the DLPNO-CCSD(T)/LED method. Intramolecular excitations occur within the same fragment. For the sake of simplicity, they are shown only for the excitations on X. Dynamic electronic preparation energy is obtained by subtracting the strong pairs energy of the isolated fragments X and Y (frozen in their in-adduct geometries) from the corresponding intramolecular terms. Only the charge transfer excitations from X to Y are shown. Analogous charge transfer excitations also exist from Y to X.

pair correlation energy of the isolated fragments) is always positive, while  $E_{C-SP}^{CT(X\rightarrow Y)}$  and  $E_{C-SP}^{CT(X\leftarrow Y)}$  are negative. These two terms typically compensate for each other to a large extent.<sup>38,40</sup> Hence, they can be combined to give the SP correlation contribution to the interaction energy excluding dispersion contribution ( $\Delta E_{no-disp}^{C-SP}$ )

$$\begin{aligned}\Delta E_{int}^{C-SP} &= (\Delta E_{el-prep}^{C-SP} + E_{C-SP}^{CT(X\rightarrow Y)} + E_{C-SP}^{CT(X\leftarrow Y)}) + E_{DISP}^{C-SP} \\ &= \Delta E_{no-disp}^{C-SP} + E_{DISP}^{C-SP}\end{aligned}\quad (17)$$

where  $\Delta E_{no-disp}^{C-SP}$  describes the correlation correction for the interaction terms approximately accounted for at the reference level (e.g., permanent and induced electrostatics).

Note that the intermolecular part of the weak-pair contribution has mainly dispersive character as it describes the correlation energy of very distant pairs of electrons. Hence, it can be added to the strong pair dispersion term  $E_{DISP}^{C-SP}$  in order to obtain the total dispersion contribution at the DLPNO-CCSD level. We label this summation as  $E_{disp}^{C-CCSD}$ . The remaining part of the correlation interaction energy at the DLPNO-CCSD level is labeled as  $\Delta E_{no-disp}^{C-CCSD}$ . Therefore

$$\Delta E_{int}^{C-CCSD} = \Delta E_{no-disp}^{C-CCSD} + E_{disp}^{C-CCSD}\quad (18)$$

Collecting all the terms we obtain for the binding energy

$$\begin{aligned}\Delta E &= \Delta E_{geo-prep} + \Delta E_{el-prep}^{ref} + E_{elstat}^{ref} + E_{exch}^{ref} + E_{disp}^{C-CCSD} \\ &+ \Delta E_{no-disp}^{C-CCSD} + \Delta E_{int}^{C-(T)}\end{aligned}\quad (19)$$

Equation 19 is the base of our LED scheme and applies identically to the closed-shell and to the open-shell cases.

As a final remark, it is worth noting that the magnitude of the single excitations term of the dynamic electronic preparation energy is typically very close to zero for closed-shell fragments due to the Brillouin's theorem. Hence, this

term provides a useful tool for localizing the fragments in which unpaired electrons are present (see Tables S5, S6, and S12).

**2.3. LED for the Analysis of Singlet–Triplet Energy Gap.** As an illustrative example of the usefulness and applicability of LED scheme, we discuss in this work the influence of the different LED components on the singlet–triplet energy gap ( $E_{S-T}$ ) of a molecule Y upon formation of a weak intermolecular interaction with X. The  $E_{S-T}$  gap of the corresponding  $^1,^3Y\cdots X$  adduct can be written as

$$E_{S-T}(Y\cdots X) = E(^1Y\cdots X) - E(^3Y\cdots X)\quad (20)$$

The same quantity for the free Y reads as

$$E_{S-T}(Y) = E(^1Y) - E(^3Y)\quad (21)$$

The variation in the singlet–triplet gap of Y upon interaction with a molecule X ( $\Delta$ ) can be obtained by subtracting eqs 20 and 21

$$\begin{aligned}\Delta &= E_{S-T}(Y\cdots X) - E_{S-T}(Y) \\ &= [E(^1Y\cdots X) - E(^3Y\cdots X)] - [E(^1Y) - E(^3Y)] \\ &= [E(^1Y\cdots X) - E(^1Y) - E(X)] - [E(^3Y\cdots X) - E(^3Y) - E(X)] \\ &= \Delta E(Y\cdots X) - \Delta E(^3Y\cdots X)\end{aligned}\quad (22)$$

Thus,  $\Delta$  equals the difference between the  $\Delta E(^1Y\cdots X)$  and  $\Delta E(^3Y\cdots X)$  binding energies. In the following, the LED scheme is used to decompose  $\Delta E(^1Y\cdots X)$  and  $\Delta E(^3Y\cdots X)$ . This approach provides insights into the physical mechanism responsible for  $\Delta$  in different systems.

### 3. COMPUTATIONAL DETAILS

All calculations were carried out with a development version of ORCA software package.<sup>43,44</sup> The presently described developments were made accessible in the ORCA 4.1 release, which is free of charge to the scientific community.

**3.1. Geometries.** The  $CH_2$  molecule and its adducts (see Figure 1) were fully optimized numerically at the DLPNO-CCSD(T) level<sup>25–34</sup> by employing the aug-cc-pVTZ basis set and its matching auxiliary counterparts.<sup>77–80</sup> We have shown on the  $CH_2\cdots He$  adduct that DLPNO-CCSD(T) gives almost identical geometries as its parent method, i.e., the canonical CCSD(T), with nonbonded interatomic distances having a maximum deviation of 0.007 Å (see Table S1 and the associated coordinates in section S1.1). The fully optimized structures of the adducts of both  $^1CH_2$  and  $^3CH_2$  at the DLPNO-CCSD(T)/aug-cc-pVTZ level are shown in Figure 1 (see section S1.1 for their coordinates).

The ferrous heme species and their CO adducts (see Figure 1) were fully optimized using the RJCOSX approximation<sup>81,82</sup> at the B3LYP<sup>83–85</sup> level incorporating the atom-pairwise dispersion correction (D3) with Becke–Johnson damping (BJ), i.e., B3LYP-D3.<sup>86</sup> The def2-TZVP basis set was used in conjunction with its matching auxiliary JK counterpart.<sup>87,88</sup> Relaxed potential energy surface (PES) scans were performed at the B3LYP-D3/def2-TZVP level for the  $PFe(^1A_{1g})\cdots CO$ ,  $PFe(^3A_{2g})\cdots CO$ , and  $PFe(^3E_g)\cdots CO$  interactions. The optimized coordinates of the  $^1A_{1g}$ ,  $^3E_g$ , and  $^3A_{2g}$  states of PFe and  $PFe\cdots CO$  (see Figure 1) at the B3LYP-D3/def2-TZVP level are given in section S2.1. It should be noted here that in the optimized structures the CO moiety is almost perpendicular to the heme plane on both singlet and triplet surfaces, consistent with previous experimental and computational studies.<sup>89–92</sup>

**Table 1.** Calculated Singlet-Triplet Energy Gap ( $E_{S-T}$ , in kcal/mol) of the Free  $\text{CH}_2$  and Its Water- and Rare Gas-Interacted Structures Together with the Variation ( $\Delta$ ) of  $E_{S-T}$  Relative to the Free  $\text{CH}_2$  at the Reference QRO/aug-cc-pV5Z, DLPNO-CCSD/TightPNO/aug-cc-pV5Z, and DLPNO-CCSD(T)/TightPNO/aug-cc-pV5Z Levels<sup>a</sup>

molecule	$E_{S-T}$		$\Delta$	
	DLPNO-CCSD(T)	DLPNO-CCSD(T)	DLPNO-CCSD	reference (QRO)
$\text{CH}_2$	9.28 <sup>b</sup>	0.00	0.00	0.00
$\text{CH}_2 \cdots \text{H}_2\text{O}$	5.57	-3.71	-3.62	-3.67
$\text{CH}_2 \cdots \text{He}$	8.97	-0.31	-0.26	0.18
$\text{CH}_2 \cdots \text{Ne}$	8.99	-0.29	-0.21	0.25
$\text{CH}_2 \cdots \text{Ar}$	8.23	-1.05	-0.76	-0.06
$\text{CH}_2 \cdots \text{Kr}$	7.40	-1.88	-1.31	2.05

<sup>a</sup>A positive (negative)  $E_{S-T}$  implies that the triplet state is more (less) stable, while the positive (negative) sign of  $\Delta$  implies the increase (decrease) in  $E_{S-T}$  of  $\text{CH}_2$  upon interacting with water and rare gases. <sup>b</sup>The corresponding canonical CCSD(T) value is 9.34 kcal/mol. Experiment including zero-point vibrational energy: 9.023 kcal/mol.<sup>102,103</sup>

**3.2. Single-Point DLPNO-CCSD(T) and LED Calculations.** DLPNO-CCSD(T) and LED calculations of both singlet and triplet states were performed with the open-shell DLPNO-CCSD(T) algorithm. Note that open-shell and closed-shell DLPNO-CCSD(T) implementations give almost identical LED energy terms for closed-shell species (see Tables S3 and S4). The distance dependence of the open-shell LED terms is given in Figure S1 for  $\text{CH}_2 \cdots \text{H}_2\text{O}$  and in section 4 for  $\text{PFe} \cdots \text{CO}$ .

Unless otherwise specified, DLPNO-CCSD(T) and LED calculations were performed using “TightPNO” settings.<sup>33,34</sup> For the heme species “NormalPNO” settings<sup>33,34</sup> with conservative TCutPairs thresholds ( $10^{-5}$ ) were also used for comparison. Hence, the so-called “NormalPNO” settings used in this study are slightly different than the standard “NormalPNO” settings. For  $\text{CH}_2 \cdots \text{H}_2\text{O}$  and heme species, the resolution-of-the-identity (RI) approach was utilized in the SCF part for both the Coulomb and the exchange terms (RIJK). For all other adducts, the RI approach was only used for the Coulomb term (RIJONX, called also as RIJDX).<sup>81,82</sup> As default in ORCA,<sup>93</sup> both geometry optimizations and single-point energy calculations at the DLPNO-CCSD(T) level were performed using the frozen-core approximation by excluding only the 1s orbital of C, N, and O, and the 1s, 2s, and 2p orbitals of Fe from the correlation treatment.

For  $\text{CH}_2$  adducts, DLPNO-CCSD(T) and LED energies were obtained with the aug-cc-pV5Z basis set. The corresponding LED terms are not affected much by the basis set size. As shown in Tables S2–S4, aug-cc-pVnZ basis sets, where  $n = \text{D, T, Q, and S}$ , provide similar results. Recently, it has been shown that the DLPNO-CCSD(T) method can be used to compute accurate singlet–triplet gaps for aryl carbenes.<sup>94</sup> On a set of 12 aryl carbenes, the mean absolute error (MAE) is only 0.2 kcal/mol.<sup>94</sup> Analogously, the MAE of the DLPNO-CCSD(T) method compared with its canonical counterpart is only 0.07 kcal/mol for binding energies and 0.04 kcal/mol for singlet–triplet energy gaps for the  $\text{CH}_2$  adducts studied in this work (see Table S5).

DLPNO-CCSD(T) and LED energies for heme species were obtained using TightPNO settings at the extrapolated complete basis set (CBS) limit by using def2-TZVP and def2-QZVP basis sets, as described previously.<sup>39,95</sup> However, for the sake of simplicity, the distance dependence of the DLPNO-CCSD(T) and LED energy terms was studied at the DLPNO-CCSD(T)/NormalPNO/def2-TZVP level. This methodology provides results that are in qualitative agreement with those obtained at the DLPNO-CCSD(T)/TightPNO/CBS level at

the equilibrium geometry (see Tables S7–S12). Note that a large number of benchmark and application studies has already shown that the DLPNO-CCSD(T)/def2-TZVP methodology typically provides a good balance between accuracy and computational cost for relative energies.<sup>35,40,96,97</sup> For triplet heme species, DLPNO-CCSD(T)/def2-TZVP binding energies are in fact very close to the estimated CBS limit (see Table S9). However, it was found that the  $\text{PFe}({}^1\text{A}_{1g}) \cdots \text{CO}$  binding energy converges slowly with the basis set size and is also quite sensitive with respect to DLPNO thresholds used (see Table S9).

For heme species, scalar relativistic effects calculated at the DLPNO-CCSD(T)/NormalPNO/def2-TZVP level by utilizing the DKH2 Hamiltonian<sup>98,99</sup> are quite small and nearly cancel out with the zero-point vibrational energy (ZPVE) calculated at the B3LYP-D3/def2-TZVP level (see Table S13). Therefore, the energies reported in the main paper are not corrected for these effects.

In DLPNO-CCSD(T) single-point energy calculations and geometry optimizations, the occupied orbitals were localized through the Foster-Boys and augmented Hessian Foster-Boys schemes, respectively.<sup>100</sup> Consistent with the closed-shell formalism,<sup>38</sup> the LED terms discussed demonstrate only a slight dependence to the localization scheme used for the occupied orbitals (see Table S6). In the LED calculations, pair natural orbitals (PNOs) were localized with the Pipek-Mezey<sup>101</sup> scheme.

Finally, it is worth mentioning that for open-shell species, QRO and UHF absolute energies differ significantly. However, the difference typically cancels out in relative energies. In the present case, QRO and UHF binding energies are essentially identical for both spin states (see Tables S5 and S7).

## 4. RESULTS AND DISCUSSION

According to eq 22, the variation ( $\Delta$ ) in the singlet–triplet gap ( $E_{S-T}$ ) of methylene upon intermolecular interaction with a molecule X is equal to the difference in the  ${}^1\text{CH}_2 \cdots \text{X}$  and  ${}^3\text{CH}_2 \cdots \text{X}$  binding energies. Analogously,  $\Delta$  in  $E_{S-T}$  of ferrous heme (PFe) upon interacting with CO is equal to the difference in the  $\text{PFe}({}^1\text{A}_{1g}) \cdots \text{CO}$  and  $\text{PFe}({}^3\text{A}_{2g}/{}^3\text{E}_g) \cdots \text{CO}$  binding energies. In the following, these binding energies are decomposed by means of the open-shell DLPNO-CCSD(T)/LED scheme. The results are then used to rationalize the different values of  $\Delta$  obtained for the different  $\text{CH}_2 \cdots \text{X}$  ( $\text{X} = \text{H}_2\text{O, He, Ne, Ar, and Kr}$ ) and  $\text{PFe} \cdots \text{CO}$  adducts studied in this work.

**4.1. CH<sub>2</sub>⋯X Interaction.** **4.1.1. Singlet–Triplet Energy Gap of CH<sub>2</sub> Adducts.** The singlet–triplet energy gap of the isolated CH<sub>2</sub> and of CH<sub>2</sub>⋯X adducts calculated at the DLPNO-CCSD(T)/TightPNO/aug-cc-pV5Z level is given in Table 1 with the computed Δ values obtained at the QRO, DLPNO-CCSD, and DLPNO-CCSD(T) levels of theory.

The triplet state of the bare CH<sub>2</sub> is calculated to be 9.28 and 9.34 kcal/mol lower in energy than its singlet state at the DLPNO-CCSD(T) and CCSD(T) levels, respectively. The inclusion of the harmonic ZPVE correction (−0.64 kcal/mol) reduces the singlet triplet gap to 8.7 kcal/mol, which is reasonably close to the experimental value of 9.023 kcal/mol.<sup>102,103</sup>

When interacting with water, the singlet–triplet gap reduces to 5.6 kcal/mol (Δ = −3.7 kcal/mol). Hence, the interaction stabilizes the singlet state more than the triplet. The largest contribution to this differential spin state stabilization comes from the reference energy, with almost no net contribution from the electron correlation term.

The interaction of CH<sub>2</sub> with rare gases is weaker than with water. At the reference level, it stabilizes the triplet more than the singlet state (Δ > 0). However, when electron correlation is incorporated, the opposite trend is observed for all adducts (Δ < 0). Importantly, Δ increases in absolute value with the polarizability of the rare gases.

The different role that electron correlation plays in the two situations above indicates that the physical mechanism responsible for the change in the singlet–triplet gap is different for methylene adducts with water and rare gases. A deeper insight into the origin of this difference comes by analyzing the <sup>1</sup>CH<sub>2</sub>⋯X and <sup>3</sup>CH<sub>2</sub>⋯X binding energies, which determine the overall Δ through eq 22. An in-depth analysis of this aspect is reported in the following by means of the LED scheme.

**4.1.2. Binding Energies of CH<sub>2</sub> Adducts.** The <sup>1</sup>CH<sub>2</sub>⋯X and <sup>3</sup>CH<sub>2</sub>⋯X binding energies are reported in Table 2. In the same table their decomposition into geometric preparation and interaction energy is also given. The latter is further

**Table 2. Calculated Equilibrium ΔE Binding Energies (kcal/mol) of the Studied CH<sub>2</sub> Adducts and Their Decomposition into the Reference (QRO/aug-cc-pV5Z) and DLPNO-CCSD(T)/TightPNO/aug-cc-pV5Z Correlation Energies Together with the Contribution Δ of Each Term to the Singlet–Triplet Gap**

molecule	state	ΔE	ΔE terms		ΔE <sub>int</sub> terms	
			ΔE <sub>int</sub>	ΔE <sub>geo-prep</sub>	ΔE <sub>int</sub> <sup>ref</sup>	ΔE <sub>int</sub> <sup>C</sup>
CH <sub>2</sub> ⋯H <sub>2</sub> O	T <sub>0</sub>	−1.56	−1.58	0.02	−0.30	−1.28
	S <sub>1</sub>	−5.27	−5.36	0.09	−3.96	−1.41
	Δ	−3.71	−3.78	0.07	−3.66	−0.13
CH <sub>2</sub> ⋯He	T <sub>0</sub>	−0.02	−0.02	0.00	0.02	−0.04
	S <sub>1</sub>	−0.33	−0.33	0.00	0.19	−0.53
	Δ	−0.31	−0.31	0.00	0.17	−0.49
CH <sub>2</sub> ⋯Ne	T <sub>0</sub>	−0.06	−0.06	0.00	0.06	−0.12
	S <sub>1</sub>	−0.35	−0.35	0.00	0.30	−0.65
	Δ	−0.29	−0.29	0.00	0.24	−0.53
CH <sub>2</sub> ⋯Ar	T <sub>0</sub>	−0.20	−0.20	0.00	0.21	−0.41
	S <sub>1</sub>	−1.25	−1.25	0.00	1.04	−2.30
	Δ	−1.05	−1.05	0.00	0.83	−1.89
CH <sub>2</sub> ⋯Kr	T <sub>0</sub>	−0.31	−0.31	0.00	0.31	−0.62
	S <sub>1</sub>	−2.19	−2.19	0.00	2.39	−4.58
	Δ	−1.88	−1.88	0.00	2.08	−3.96

decomposed into its reference and correlation energy contributions.

Consistent with the trend of Δ previously discussed, water and rare gases interact more strongly with <sup>1</sup>CH<sub>2</sub> than with <sup>3</sup>CH<sub>2</sub>, thus resulting in a lowering of the singlet–triplet gap in CH<sub>2</sub>⋯X compounds (Δ < 0). The extent of the ΔE<sub>int</sub><sup>ref</sup> and ΔE<sub>int</sub><sup>C</sup> contributions to the <sup>1</sup>CH<sub>2</sub>⋯X and <sup>3</sup>CH<sub>2</sub>⋯X interactions varies depending on the system. In particular, ΔE<sub>int</sub><sup>ref</sup> dominates the CH<sub>2</sub>⋯H<sub>2</sub>O interaction, while the CH<sub>2</sub>⋯Rg interaction is dominated by ΔE<sub>int</sub><sup>C</sup>. The ΔE<sub>int</sub><sup>ref</sup> and ΔE<sub>int</sub><sup>C</sup> contributions of the <sup>1,3</sup>CH<sub>2</sub>⋯X interactions are decomposed with the LED scheme into physically meaningful terms. The corresponding LED energy terms at the equilibrium geometries are reported in Table 3 and discussed in the next section.

**4.1.3. LED Analysis of the CH<sub>2</sub>⋯H<sub>2</sub>O Interaction.** For the <sup>3</sup>CH<sub>2</sub>⋯H<sub>2</sub>O case, the sum of attractive electrostatic E<sub>elstat</sub> and exchange E<sub>exch</sub> terms of ΔE<sub>int</sub><sup>ref</sup> is almost entirely compensated by its repulsive static electronic preparation term ΔE<sub>el-prep</sub><sup>ref</sup> (see Table 3). Thus, ΔE<sub>int</sub><sup>ref</sup> is practically negligible, demonstrating that dynamic electron correlation is responsible for the stability of the <sup>3</sup>CH<sub>2</sub>⋯H<sub>2</sub>O adduct. In particular, London dispersion is one of the most important energy components of the interaction, as demonstrated by the large E<sub>disp</sub><sup>C-CCSD</sup>/ΔE ratio of 0.57.

A different picture emerges in <sup>1</sup>CH<sub>2</sub>⋯H<sub>2</sub>O. In this case, the interacting species are closer (see Figure 1) and ΔE<sub>int</sub><sup>ref</sup> consists of larger ΔE<sub>el-prep</sub><sup>ref</sup> and E<sub>elstat</sub> values compared with those of <sup>3</sup>CH<sub>2</sub>⋯H<sub>2</sub>O. These two contributions largely cancel each other. Hence, the overall ΔE<sub>int</sub><sup>ref</sup> is on the order of the remaining attractive exchange interaction.

Even though the correlation contribution to the <sup>1,3</sup>CH<sub>2</sub>⋯H<sub>2</sub>O interaction is largely dominated by the London dispersion term E<sub>disp</sub><sup>C-CCSD</sup> (see Table 3) and significantly contributes to the intermolecular interaction, its magnitude is almost identical for both spin states. Hence, the decrease in the singlet–triplet gap of CH<sub>2</sub> while interacting with water is driven by the fact that <sup>1</sup>CH<sub>2</sub>⋯H<sub>2</sub>O shows a much larger electrostatic interaction than <sup>3</sup>CH<sub>2</sub>⋯H<sub>2</sub>O.

This effect can be simply rationalized by looking at the schematic representation of the electronic configuration of singlet (Figure 3, top left) and triplet (Figure 3, top right) carbenes,<sup>104</sup> reported in Figure 3. At the bottom of the same figure, their molecular electrostatic potential (MEP)<sup>105</sup> maps projected onto the corresponding one electron densities at the reference level are also reported. The MEP map of the singlet methylene (Figure 3, bottom left) shows a negative electrostatic potential in the region of the lone pair. This favors H-bond interactions. Conversely, the MEP of the triplet carbene is much more isotropic, which leads to weaker H-bonding interactions.

It is worth mentioning here that the singles term included in ΔE<sub>no-disp</sub><sup>C-CCSD</sup> amounts to −2.4 kcal/mol for the <sup>3</sup>CH<sub>2</sub> fragment of all of the adducts studied in this work (see Table S5). In contrast, the adducts containing <sup>1</sup>CH<sub>2</sub> features a negligible singles term (the Brillouin's theorem is satisfied in this case). In general, the magnitude of the singles term can be used to identify the fragment in which the unpaired electron is localized.

**4.1.4. LED Analysis of the CH<sub>2</sub>⋯Rg Interaction.** The interaction of CH<sub>2</sub> with rare gases is relatively weak. In both singlet and triplet states (see Tables 2 and 3), the ΔE<sub>int</sub><sup>ref</sup> values are positive, meaning that the repulsive electronic preparation

**Table 3.** LED of the Reference (QRO/aug-cc-pV5Z) and DLPNO-CCSD(T)/TightPNO/aug-cc-pV5Z Correlation Contributions to Interaction Energies (kcal/mol) for the Studied CH<sub>2</sub> Adducts and the Contribution  $\Delta$  of Each Term to the Singlet–Triplet Gap

molecule	state	reference energy decomposition				correlation energy decomposition				
		$\Delta E_{\text{int}}^{\text{ref}}$	$\Delta E_{\text{el-prep}}^{\text{ref}}$	$E_{\text{elstat}}$	$E_{\text{exch}}$	$\Delta E_{\text{int}}^{\text{C}}$	$E_{\text{disp}}^{\text{C-CCSD}}$	$\Delta E_{\text{no-disp}}^{\text{C-CCSD}}$	$\Delta E_{\text{int}}^{\text{C-(T)}}$	$\frac{E_{\text{disp}}^{\text{C-CCSD}}}{\Delta E}$
CH <sub>2</sub> ⋯H <sub>2</sub> O	T <sub>0</sub>	-0.30	20.71	-15.88	-5.13	-1.28	-0.89	-0.23	-0.16	0.57
	S <sub>1</sub>	-3.96	29.71	-28.70	-4.96	-1.41	-1.22	0.04	-0.23	0.23
	$\Delta$	-3.66	9.00	-12.82	0.17	-0.13	-0.33	0.27	-0.07	0.09
CH <sub>2</sub> ⋯He	T <sub>0</sub>	0.02	0.09	-0.06	-0.03	-0.04	-0.05	0.01	0.00	2.50
	S <sub>1</sub>	0.19	1.39	-0.78	-0.43	-0.53	-0.44	-0.04	-0.05	1.33
	$\Delta$	0.17	1.30	-0.72	-0.40	-0.49	-0.39	-0.05	-0.05	1.26
CH <sub>2</sub> ⋯Ne	T <sub>0</sub>	0.06	0.69	-0.54	-0.13	-0.12	-0.12	0.01	-0.01	2.00
	S <sub>1</sub>	0.30	2.63	-1.85	-0.52	-0.65	-0.58	0.01	-0.08	1.66
	$\Delta$	0.24	1.94	-1.31	-0.39	-0.53	-0.46	0.00	-0.07	1.59
CH <sub>2</sub> ⋯Ar	T <sub>0</sub>	0.21	3.18	-2.36	-0.55	-0.41	-0.39	0.02	-0.04	1.95
	S <sub>1</sub>	1.04	11.69	-8.00	-2.60	-2.30	-1.65	-0.31	-0.34	1.32
	$\Delta$	0.83	8.51	-5.64	-2.05	-1.89	-1.26	-0.33	-0.30	1.20
CH <sub>2</sub> ⋯Kr	T <sub>0</sub>	0.31	1.68	-4.27	-0.88	-0.62	-0.48	-0.09	-0.05	1.55
	S <sub>1</sub>	2.39	27.78	-22.53	-6.63	-4.58	-2.67	-1.30	-0.61	1.22
	$\Delta$	2.08	26.1	-18.26	-5.75	-3.96	-2.19	-1.21	-0.56	1.16

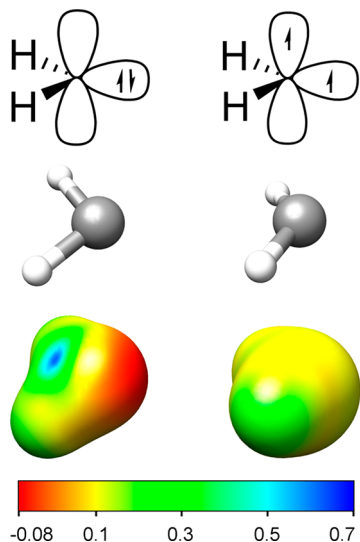


**Figure 3.** Valence electron configurations and molecular electrostatic potential maps of <sup>1</sup>CH<sub>2</sub> (left) and <sup>3</sup>CH<sub>2</sub> (right) projected onto the corresponding molecular electron densities calculated at the UHF/aug-cc-pV5Z level in the unit of  $E_{\text{h}}/e$ . Red region identifies lowest electrostatic potential and thus highest electron density, while blue region identifies the opposite.

energies due to the distortion of electron clouds of both CH<sub>2</sub> and rare gases dominate over the sum of the attractive electrostatic and exchange interactions. Hence, the overall  $\Delta E$  is dominated by electron correlation and, in particular, by the London dispersion contribution ( $E_{\text{disp}}^{\text{C-CCSD}}/\Delta E > 1.5$ ).

It is worth mentioning here that the first explanation of the attraction between two nonpolar molecules was given by F. London.<sup>106,107</sup> An approximated expression for the London dispersion energy between two atoms (X and Y), i.e.,  $E_{\text{disp,L}}$  can be written

$$E_{\text{disp,L}} = -\frac{C_6}{r^6} = -\frac{3 \cdot I_X \cdot I_Y \cdot \alpha_X \cdot \alpha_Y}{2 \cdot (I_X + I_Y) \cdot r^6} \quad (23)$$

where  $C_6$  is the atom pairwise induced dipole–induced dipole interaction coefficient,  $I_X$  and  $I_Y$  are the first ionization potential of the interacting X and Y molecules,  $\alpha_X$  and  $\alpha_Y$  are the polarizabilities of X and Y, and  $r$  is the distance between X and Y.

It can be assessed how well this simple London equation quantifies the dispersion interaction energy between CH<sub>2</sub> and rare gases by comparing the London dispersion energies obtained from eq 23 with those derived from the LED method. To do that we computed ionization potential and numerical polarizabilities of the isolated CH<sub>2</sub> and rare gas atoms at the DLPNO-CCSD(T)/aug-cc-pV5Z level. The computed values are reasonably close to the available experimental values (see Table 4).<sup>108–114</sup> As an approximation we take  $r$  as the distance between the rare gas and the carbon atom (see Figure 1) at the equilibrium geometry of CH<sub>2</sub>⋯Rg adducts.

**Table 4.** Numerical DLPNO-CCSD(T)/TightPNO/aug-cc-pV5Z Polarizabilities ( $\alpha$ ) and the Ionization Potentials ( $I$ ) Compared with Available Experimental Data

	state	$\alpha_{\text{calc}}$ ( $\text{\AA}^3$ )	$\alpha_{\text{exp}}$ ( $\text{\AA}^3$ ) <sup>108–110</sup>	$I_{\text{calc}}$ (eV)	$I_{\text{exp}}$ (eV) <sup>111–114</sup>
CH <sub>2</sub>	T <sub>0</sub>	2.186		10.393	10.386
CH <sub>2</sub>	S <sub>1</sub>	2.391		10.599	
H <sub>2</sub> O	S <sub>0</sub>	1.449	1.456	12.753	12.621
He	S <sub>0</sub>	0.205	0.205	24.442	24.587
Ne	S <sub>0</sub>	0.393	0.395	21.572	21.565
Ar	S <sub>0</sub>	1.642	1.643	15.784	15.760
Kr	S <sub>0</sub>	2.475	2.486	14.200	14.000

The correlation between the dispersion energies obtained with London formula and the corresponding LED values for the CH<sub>2</sub>⋯Rg systems studied in this work is given in Figure 4. Despite the simplicity of the London equation and the various approximations adopted, the dispersion energy estimates obtained with the two methods show a reasonably good linear correlation, with an  $R^2$  larger than 0.98 for both the <sup>1</sup>CH<sub>2</sub>⋯Rg and the <sup>3</sup>CH<sub>2</sub>⋯Rg series. In all cases, London dispersion increases with the increase of the polarizability of the rare gas atoms.



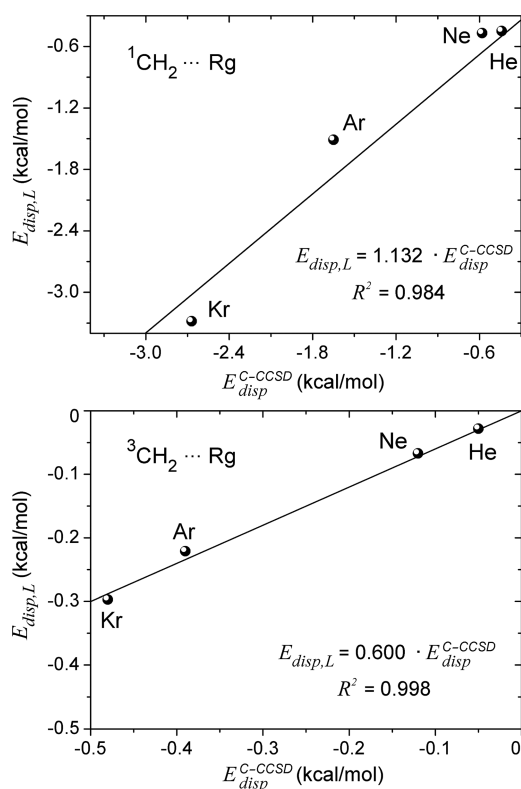


**Figure 4.** Plot of dispersion energies of  $\text{CH}_2$  interacting with rare gases:  $E_{\text{disp}}^{\text{C-CCSD}}$  of DLPNO-CCSD(T)/TightPNO/LED/aug-cc-pV5Z vs  $E_{\text{disp,L}}$  of London equation.

The  $^1\text{CH}_2\cdots\text{Rg}$  dispersion energies obtained by the London formula are very similar to the LED values, with variations of 13% in average. On the other hand, the London formula underestimates (−40%) the  $^3\text{CH}_2\cdots\text{Rg}$  dispersion interaction. The incorporation of the higher order terms seems thus necessary for open-shell systems in order to estimate dispersion energies more accurately.

**4.2. Ferrous Heme...CO Interaction.** **4.2.1. Relative Spin State Energies of Heme Species.** The calculated singlet–triplet ( $^1\text{A}_{1g} - ^3\text{E}_g$  and  $^1\text{A}_{1g} - ^3\text{A}_{2g}$ ) and triplet–triplet ( $^3\text{E}_g - ^3\text{A}_{2g}$ ) energy gaps of the free and CO-bound heme are given in

Table 5 at various levels of theory. The corresponding  $\Delta$  values are also reported in the same table.

Experimental studies on bare iron–porphyrin (see ref 115 for a review) agree on its ground-state multiplicity (triplet) but differ in the interpretation of the ground-state electronic configuration. In particular, Mössbauer data of iron(II)–tetraphenylporphyrin (FeTPP) were interpreted as an indication of either a  $^3\text{E}_g$ <sup>116</sup> or a  $^3\text{A}_{2g}$ <sup>70,117</sup> ground state. Ligand field calculations that are consistent with the magnetic susceptibility measurements predict an  $^3\text{A}_{2g}$  ground state.<sup>118</sup> Consistently, previous hybrid density functional, CASPT2, and several CI studies find the  $^3\text{A}_{2g}$  state more stable than the  $^3\text{E}_g$  state by 2 kcal/mol or less.<sup>89,115</sup> Consistently, the present B3LYP-D3/def2-TZVP and DLPNO-CCSD(T)/TightPNO/CBS calculations find the  $^3\text{A}_{2g}$  state of heme to be only 0.96 and 1.97 kcal/mol more stable than the  $^3\text{E}_g$  state, respectively (see Table 5).

The  $d_z^2$  orbital of Fe(II), which is doubly occupied in the  $^3\text{A}_{2g}$  state, is destabilized upon the binding of an axial ligand to the ferrous heme.<sup>89,119</sup> The amount of this destabilization and thus spin-state energetics depends strongly on the nature of the axial ligand. For example, upon imidazole binding, the  $d_z^2$  orbital raises in energy and becomes singly occupied. Thus, the ground state changes from triplet to quintet, and the lowest triplet changes from  $^3\text{A}_{2g}$  to  $^3\text{E}_g$ .<sup>89</sup> As CO is a strong field ligand, the destabilization of the  $d_z^2$  orbital upon its binding to heme is even larger. In fact, PFe–CO systems having side chains feature a singlet ground state with a formally empty  $d_z^2$  orbital.<sup>67</sup> Consequently, the identity of the most stable triplet state of CO-bound heme complexes is rarely studied. The present calculations find the  $^3\text{E}_g$  state of the CO-bound heme to be 2.16 and 0.57 kcal/mol more stable than  $^3\text{A}_{2g}$  at the B3LYP-D3/def2-TZVP and DLPNO-CCSD(T)/TightPNO/CBS levels, respectively. Hence, CO binding probably reverses the energetic order of the  $^3\text{E}_g$  and  $^3\text{A}_{2g}$  states, consistent with the imidazole-bound heme case. These changes can be rationalized in terms of the destabilization of the  $d_z^2$  orbital of Fe(II).

Unfortunately, no direct experimental measure of  $E_{\text{S-T}}$  gaps exists for these complexes. At the B3LYP-D3/def2-TZVP and DLPNO-CCSD(T)/TightPNO/CBS levels, the  $E_{\text{S-T}}$  gap of the free heme is 33.32 and 32.13 kcal/mol relative to  $^3\text{E}_g$  while

**Table 5.** Calculated Relative Spin State Energies ( $E_{\text{rel}}$ ) of the Free and CO-Bound Heme Together with the Variation ( $\Delta$ ) of  $E_{\text{rel}}$  Relative to the Free Heme at the Reference QRO/CBS, DLPNO-CCSD(T)/TightPNO/CBS, and DLPNO-CCSD(T)/TightPNO/CBS Levels (in kcal/mol)<sup>a</sup>

	$E_{\text{rel}}$		$\Delta$	
	DLPNO-CCSD(T)	DLPNO-CCSD(T)	DLPNO-CCSD	reference (QRO)
$^3\text{E}_g - ^3\text{A}_{2g}$ <sup>a</sup>				
PFe	1.97	0.00	0.00	0.00
PFe...CO	−0.57	−2.54	−1.24	6.67
$^1\text{A}_{1g} - ^3\text{E}_g$ <sup>b</sup>				
PFe	32.13	0.00	0.00	0.00
PFe...CO	−6.50	−38.63	−31.78	9.10
$^1\text{A}_{1g} - ^3\text{A}_{2g}$ <sup>b</sup>				
PFe	34.10	0.00	0.00	0.00
PFe...CO	−7.07	−41.17	−33.02	15.77

<sup>a</sup>A positive (negative)  $E_{\text{rel}}$  implies that the  $^3\text{A}_{2g}$  state is more (less) stable than the  $^3\text{E}_g$ , while the negative (positive) sign of  $\Delta$  implies the increase (decrease) in the stability of the  $^3\text{E}_g$  state relative to the  $^3\text{A}_{2g}$  state of PFe upon interacting with CO. <sup>b</sup>In this case,  $E_{\text{rel}}$  corresponds to  $E_{\text{S-T}}$ . A positive (negative)  $E_{\text{rel}}$  implies that the triplet state is more (less) stable than the singlet state, while the positive (negative) sign of  $\Delta$  implies the increase (decrease) in  $E_{\text{S-T}}$  of PFe upon interacting with CO.

it is 34.88 and 34.10 kcal/mol relative to  $^3A_{2g}$  (see Table 5). As detailed in Table S7, these figures are only weakly affected by the technical parameters of the calculations and are consistent with those obtained previously at the CASPT2 level (~35 kcal/mol).<sup>89</sup>

As seen in Table 5, upon interacting with CO, at the DLPNO-CCSD(T)/TightPNO/CBS level, the  $E_{S-T}$  gap relative to the  $^3E_g$  and  $^3A_{2g}$  states reduces to  $-6.50$  and  $-7.07$  kcal/mol ( $\Delta = -38.63$  and  $-41.17$  kcal/mol), respectively. Hence, CO binding significantly stabilizes the  $^1A_{1g}$  state (which becomes the ground state), consistent with the above-mentioned experimental findings on related systems. An in-depth discussion of the physical mechanism behind this differential spin state stabilization is reported in the following sections.

**4.2.2. Binding Energy of the Heme Adducts.** The calculated binding energies of  $PFe(^1A_{1g})\cdots CO$ ,  $PFe(^3E_g)\cdots CO$ , and  $PFe(^3A_{2g})\cdots CO$  adducts at the DLPNO-CCSD(T)/TightPNO/CBS level are reported in Table 6. In the same

**Table 6. Calculated Equilibrium  $\Delta E$  Binding Energies (kcal/mol) of the CO-Bound Heme Adducts and Their Decomposition into the Reference (QRO/CBS) and DLPNO-CCSD(T)/TightPNO/CBS Correlation Energies Together with the Contribution  $\Delta$  of Each Term to the Singlet–Triplet Energy Gap**

	$\Delta E$	$\Delta E$ terms		$\Delta E_{int}$ terms	
		$\Delta E_{int}$	$\Delta E_{geo-prep}$	$\Delta E_{int}^{ref}$	$\Delta E_{int}^C$
$^3E_g$	-4.21	-5.94	1.74	7.31	-13.25
$^3A_{2g}$	-1.67	-1.77	0.10	1.06	-2.84
$^1A_{1g}$	-42.84	-46.28	3.44	12.28	-58.55
$\Delta^1A_{1g}-^3E_g$	-38.63	-40.34	1.70	4.97	-45.30
$\Delta^1A_{1g}-^3A_{2g}$	-41.17	-44.51	3.34	11.22	-55.71

table, their decomposition into geometric preparation and interaction energy is also given. The latter is further decomposed into reference and correlation energy contributions.

The  $PFe(^1A_{1g})\cdots CO$  interaction is much stronger than the  $PFe(^3A_{2g}/^3E_g)\cdots CO$  ones, as apparent from their large negative  $\Delta$  values of  $-41.17/-38.63$  kcal/mol (see Table 6). This leads to the observed reduction of the singlet–triplet gap of heme derivatives shown in Table 5. However, at the reference level, the  $PFe(^1A_{1g})\cdots CO$  interaction is strongly repulsive ( $\Delta E_{int}^{ref} > 0$ ). Thus, electron correlation counteracts this repulsion in the singlet state and makes the overall interaction significantly attractive.

On the technical side,  $PFe(^3E_g/^3A_{2g})\cdots CO$  binding energies do not depend significantly on the computational settings used

in the DLPNO-CCSD(T) calculations. In contrast, the binding energy of the  $PFe(^1A_{1g})\cdots CO$  adduct is more sensitive to the DLPNO thresholds and basis sets (see Table S8) adopted. For example, the  $PFe(^1A_{1g})\cdots CO$  binding energy is  $-42.84$  kcal/mol with TightPNO/CBS and  $-36.90$  kcal/mol with NormalPNO/def2-TZVP settings. Hence, NormalPNO/def2-TZVP settings should only be used if one is interested in mechanistic tendencies rather than in accurate quantitative estimates of binding energies of heme species.

The  $PFe(^1A_{1g})\cdots CO$  binding energy calculated at the DLPNO-CCSD(T)/TightPNO/CBS ( $-42.84$  kcal/mol), B3LYP-D3/def2-TZVP ( $-46.95$  kcal/mol), and CASPT2<sup>89</sup> ( $-51.3$  kcal/mol) levels varies significantly. Relative to the ground  $PFe(^3A_{2g})$  state, these estimates are  $-8.74$ ,  $-12.67$ , and  $-16.4$  kcal/mol, respectively. As already mentioned, experimental data are not available for this system. The only experimentally determined binding energy on a related system was obtained for a heme derivative in which four tetrakis(4-sulfonatophenyl) anions (tpps) are bound to the four meso carbons of porphyrin connecting pyrrole moieties. In this case, the experimental gas-phase binding energy of the  $PFe(^1A_{1g})-CO$  adduct was measured to be  $-15.85$  kcal/mol relative to the ground state of  $PFe$ .<sup>120</sup> It is worth stressing here that the four tpps anions (i.e., a total charge of  $-4$ ) bend the porphyrin moiety significantly and thus are expected to alter the electronic structure of the system as well. In fact, the binding energy of this system is predicted to be 2.05 kcal/mol larger in absolute value than that of side chain free  $PFe(^1A_{1g})\cdots CO$  at the B3LYP-D3/def2-TZVP level of theory.

**4.2.3. LED Analysis of the Interaction between Heme and CO.** LED terms of the  $PFe(^1A_{1g}/^3E_g/^3A_{2g})\cdots CO$  interactions are given in Table 7 at the DLPNO-CCSD(T)/TightPNO/CBS level. For an in-depth analysis of these interactions, we also performed DLPNO-CCSD(T)/NormalPNO/def2-TZVP single-point energy calculations on a series of structures obtained from constrained B3LYP-D3 geometry optimizations in which the Fe–C distance ( $r_{Fe\cdots C}$ ) was varied from  $\sim 1.7$  to  $\sim 4.5$  Å with an increment of 0.2 Å. The resulting energy profiles are reported in Figure 5 together with their decomposition into the various LED terms.

As mentioned above,  $PFe(^3A_{2g})$  features a doubly occupied  $d_z^2$  orbital that points toward the CO lone pair located on the carbon atom, while in  $PFe(^3E_g)$  the  $d_z^2$  orbital is singly occupied. For this reason,  $PFe(^3A_{2g})\cdots CO$  features a steeper repulsive wall than  $PFe(^3E_g)\cdots CO$ . This leads to a longer Fe–C bond distance in  $PFe(^3A_{2g})\cdots CO$  (3.27 Å) than in  $PFe(^3E_g)\cdots CO$  (2.29 Å). Accordingly, the  $PFe(^3A_{2g})\cdots CO$  interaction ( $-1.67$  kcal/mol) is weaker than the  $PFe(^3E_g)\cdots CO$  one ( $-4.21$  kcal/mol), and all of the LED terms of  $PFe(^3A_{2g})\cdots CO$  are smaller than those of  $PFe(^3E_g)\cdots CO$  at the

**Table 7. LED of the Reference (QRO/CBS) and DLPNO-CCSD(T)/TightPNO/CBS Correlation Interaction Energies (kcal/mol) for the CO-Bound Heme Adducts and the Contribution  $\Delta$  of Each Term to the Singlet–Triplet Gap**

	reference energy decomposition				correlation energy decomposition				
	$\Delta E_{int}^{ref}$	$\Delta E_{el-prep}^{ref}$	$E_{elstat}$	$E_{exch}$	$\Delta E_{int}^C$	$E_{disp}^{C-CCSD}$	$\Delta E_{no-disp}^{C-CCSD}$	$\Delta E_{int}^{C(T)}$	$\frac{E_{disp}^{C-CCSD}}{\Delta E}$
$^3E_g$	7.31	153.39	-121.54	-24.54	-13.25	-7.53	-4.11	-1.61	1.79
$^3A_{2g}$	1.06	12.94	-9.67	-2.21	-2.84	-2.61	0.07	-0.29	1.56
$^1A_{1g}$	12.28	714.55	-601.76	-100.51	-58.55	-22.56	-27.88	-8.11	0.53
$\Delta^1A_{1g}-^3E_g$	4.97	561.16	-480.22	-75.97	-46.30	-15.03	-23.77	-6.50	0.39
$\Delta^1A_{1g}-^3A_{2g}$	11.22	701.61	-592.09	-98.3	-55.71	-19.95	-27.95	-7.82	0.48

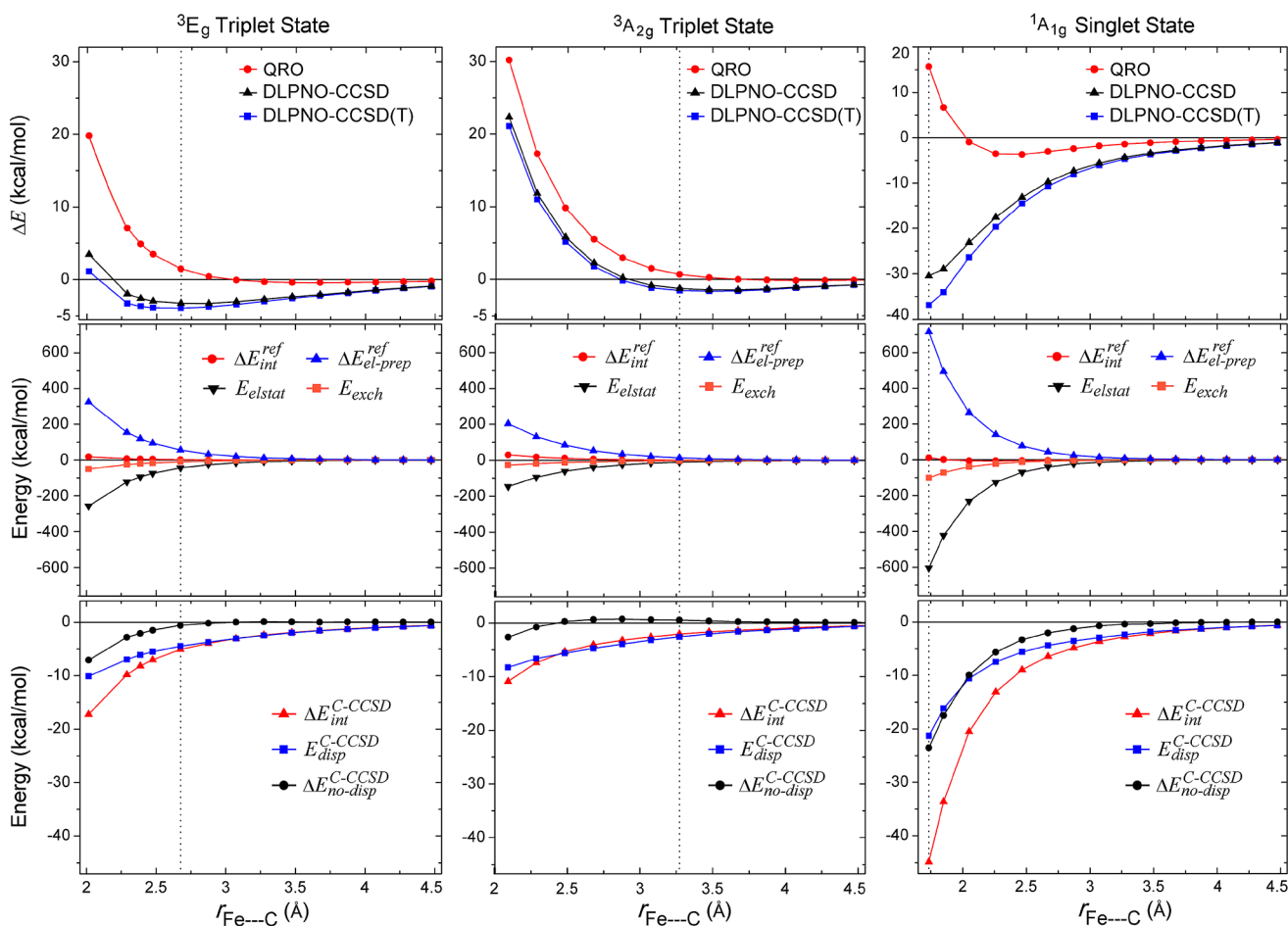


**Figure 5.** Distance dependence of DLPNO-CCSD(T)/NormalPNO/LED/def2-TZVP terms of the interaction of CO with the  $^3E_g$  triplet (left),  $^3A_{2g}$  triplet (middle), and  $^1A_{1g}$  singlet (right) states of PFe at the B3LYP-D3/def2-TZVP geometries. Relaxed PES scans were performed at the B3LYP-D3/def2-TZVP level. Vertical dotted lines correspond to the B3LYP-D3 minima. Energy of the dissociated fragments is used as reference in all cases.

B3LYP-D3 equilibrium geometry (see Tables 6 and 7, and Tables S9–S11).

For both triplet states, the interaction between PFe( $^3E_g/^3A_{2g}$ ) and CO is repulsive at the QRO level (top panels of Figure 5 and Table 7) in the short range. Consistent with this picture, the LED decomposition of the reference PFe( $^3E_g/^3A_{2g}$ )...CO interaction energies (central panels of Figure 5 and Table 7) shows that the repulsive electronic preparation energies due to the distortion of the electron clouds of PFe( $^3E_g/^3A_{2g}$ ) and CO are always larger or approximately equal in magnitude than the sum of the attractive electrostatic and exchange interaction energies.

Hence, dynamic electron correlation is essential to the stability of PFe( $^3E_g/^3A_{2g}$ )...CO adducts. Note that the B3LYP-D3 equilibrium geometries for the PFe( $^3E_g/^3A_{2g}$ )...CO adducts feature shorter intermolecular distances (of about 0.6/0.2 Å) than the DLPNO-CCSD(T) minima. However, this has only a small impact on the DLPNO-CCSD(T) binding energy due to the flatness of the PES.

The decomposition of the correlation binding energy (see bottom panels of Figure 5 and Table 7) shows that the dispersion energy dominates the PFe( $^3E_g/^3A_{2g}$ )...CO interaction. The corresponding  $E_{\text{disp}}^{\text{C-CCSD}}$  value amounts to  $-7.53/-2.61$  kcal/mol at the B3LYP-D3 equilibrium geometry. In fact, both PFe( $^3E_g$ )...CO and PFe( $^3A_{2g}$ )...CO adducts have a

$E_{\text{disp}}^{\text{C-CCSD}}/\Delta E$  ratio larger than 1.5 (see Tables 7 and S11) and can be both described as a van der Waals adduct mainly stabilized by London dispersion forces.

By contrast, the nature of the PFe( $^1A_{1g}$ )...CO interaction is completely different. The energy profile computed at the QRO level (top right panel of Figure 5) shows a shallow minimum at about 2.5 Å. The corresponding DLPNO-CCSD(T) energy profile shows a very deep minimum (NormalPNO/def2-TZVP,  $-36.90$  kcal/mol; TightPNO/CBS,  $-42.84$  kcal/mol) at  $\sim 1.7$  Å, where the QRO interaction energy is repulsive. Thus, electron correlation affects significantly both the stability and the geometry of the PFe( $^1A_{1g}$ )...CO adduct.

The LED decomposition of the reference PFe( $^1A_{1g}$ )...CO interaction energy (central right panel of Figure 5) shows that the electrostatic interaction is larger than the corresponding electronic preparation at the QRO minimum. Importantly, the PFe( $^1A_{1g}$ )...CO interaction at the QRO level is associated with larger LED components for both repulsive and attractive terms than the PFe( $^3E_g/^3A_{2g}$ )...CO interaction at all Fe–C distances. Hence, the electronic clouds of the interacting fragments are distorted more significantly and interact stronger in PFe( $^1A_{1g}$ )...CO than in PFe( $^3E_g/^3A_{2g}$ )...CO, indicating that a significant polarization of the fragments occurs upon CO binding already at the QRO level.

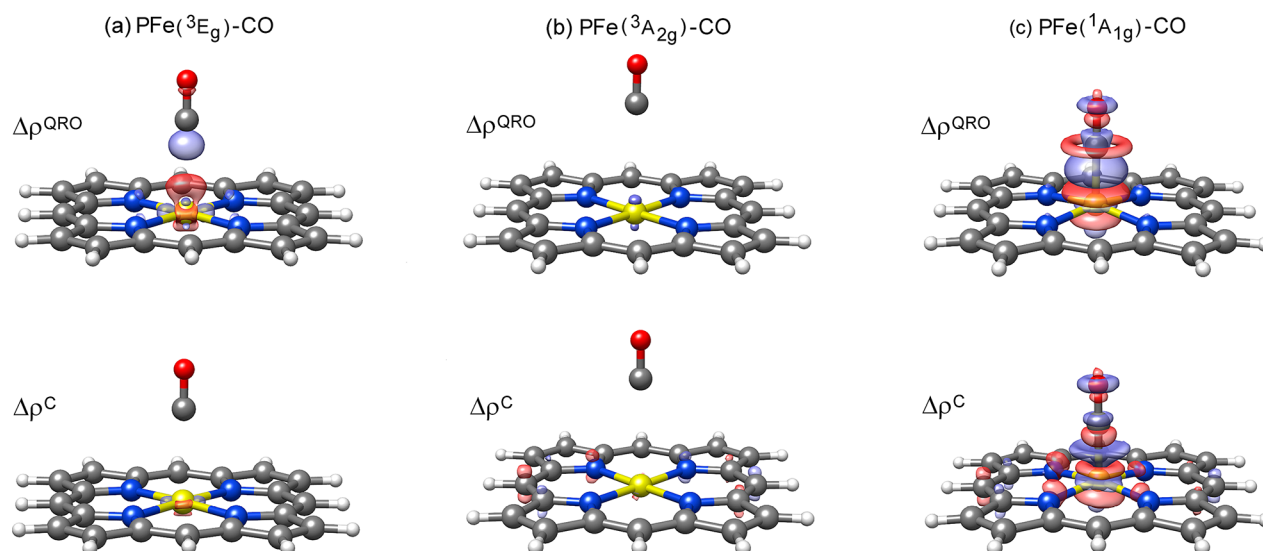


**Figure 6.** For (a)  ${}^3E_g$ , (b)  ${}^3A_{2g}$ , and (c)  ${}^1A_{1g}$  states, the contour plots of the reference QRO (up) and the DLPNO-CCSD/NormalPNO/def2-TZVP correlation (bottom) contributions to the electron density rearrangements taking place upon CO binding. Plots are all given with the density isosurface contour value of  $\pm 0.002 e/\text{Bohr}^3$ . Blue and red surfaces identify regions of electron density accumulation and depletion, respectively.

The analysis of the LED terms of the correlation energy reported in the bottom right panel of Figure 5 is illuminating. Dispersive, nondispersive, and triples contribution are all significant in the short range. The corresponding TightPNO/CBS values at the B3LYP-D3 equilibrium geometry are  $-22.56$ ,  $-27.88$ , and  $-8.11$  kcal/mol for  $E_{\text{disp}}^{C-\text{CCSD}}$ ,  $\Delta E_{\text{no-disp}}^{C-\text{CCSD}}$ , and  $\Delta E_{\text{int}}^{C-\text{(T)}}$ , respectively. Hence, these three correlation terms are responsible for the significant strength of the  $\text{PFe}({}^1A_{1g})\cdots\text{CO}$  interaction, which in turn determines the reduction observed in the singlet–triplet gap of PFe upon CO binding. In particular, the large magnitude of the nondispersive component suggests that electron correlation significantly affects the polarization of the interacting fragments.<sup>6</sup>

To analyze this aspect in more detail, we obtained 3D contour plots of the one electron density difference function  $\Delta\rho(x,y,z)$  describing the electron density rearrangement taking place upon CO binding for each spin state. The  $\Delta\rho(x,y,z)$  function is computed as the difference between the electron density of the  $\text{PFe}\cdots\text{CO}$  adduct (for a given spin state) and the sum of the electron densities of PFe (at the same spin state) and CO frozen at their in-adduct geometries. In order to investigate electron correlation effects to the  $\text{PFe}\cdots\text{CO}$  binding,  $\Delta\rho$  was divided into a reference ( $\Delta\rho^{\text{QRO}}$ ) and an unrelaxed DLPNO-CCSD correlation ( $\Delta\rho^{\text{C}}$ ) contribution calculated via the solution of  $\Lambda$  equations.<sup>121,122</sup> The corresponding contour plots are shown in Figure 6.

Consistent with the fact that the LED describes the  $\text{PFe}({}^3E_g/{}^3A_{2g})\cdots\text{CO}$  adducts as van der Waals complexes held together by London dispersion, the corresponding  $\Delta\rho^{\text{QRO}}$  and  $\Delta\rho^{\text{C}}$  contour plots show that only a small charge rearrangement takes place upon bond formation in the triplet states. In contrast, the  $\text{PFe}({}^1A_{1g})\cdots\text{CO}$  interaction is accompanied by a significant charge accumulation in the region of the bond, consistent with the fact that the  $\text{PFe}({}^1A_{1g})\cdots\text{CO}$  interaction is associated with larger electrostatic, exchange, and electronic preparation energy components. This is evident from the contour plots of the corresponding  $\Delta\rho^{\text{QRO}}$  and  $\Delta\rho^{\text{C}}$  functions and consistent with the fact that the  $\text{PFe}({}^1A_{1g})\cdots\text{CO}$  interaction is associated with a large nondispersive correlation term.

The contour plots just discussed are consistent with the variations in d-orbital populations occurring upon CO binding ( $\Delta q$ ) reported in Table 8. The  $\Delta q$  values are negligible for all d

**Table 8.** UHF/def2-TZVP and DLPNO-CCSD/NormalPNO/def2-TZVP Mulliken d-Orbital Populations ( $q$  in Units of  $e$ ) for the  ${}^3E_g$ ,  ${}^3A_{2g}$ , and  ${}^1A_{1g}$  States of PFe and  $\text{PFe}\cdots\text{CO}$  Together with Their Variations Upon CO Binding ( $\Delta q$ )

	UHF			DLPNO-CCSD		
	$q_{\text{PFe}}$	$q_{\text{PFe}\cdots\text{CO}}$	$\Delta q$	$q_{\text{PFe}}$	$q_{\text{PFe}\cdots\text{CO}}$	$\Delta q$
${}^3E_g$						
$d_z^2$	1.15	1.15	0.00	1.13	1.14	0.01
$d_{xz}$	1.02	1.02	0.00	1.03	1.03	0.00
$d_{yz}$	2.00	2.00	0.00	1.98	1.98	0.00
$d_{x^2-y^2}$	1.89	1.87	-0.02	1.91	1.87	-0.04
$d_{xy}$	0.36	0.36	0.00	0.48	0.48	0.00
${}^3A_{2g}$						
$d_z^2$	1.96	1.97	0.01	1.93	1.94	0.01
$d_{xz}$	1.02	1.02	0.00	1.03	1.02	-0.01
$d_{yz}$	1.02	1.02	0.00	1.03	1.02	-0.01
$d_{x^2-y^2}$	2.00	2.00	0.00	1.99	1.99	0.00
$d_{xy}$	0.36	0.36	0.00	0.49	0.49	0.00
${}^1A_{1g}$						
$d_z^2$	0.07	0.22	0.15	0.11	0.40	0.29
$d_{xz}$	2.01	1.93	-0.08	1.99	1.84	-0.15
$d_{yz}$	2.01	1.93	-0.08	1.99	1.84	-0.15
$d_{x^2-y^2}$	2.00	2.02	0.02	1.99	2.01	0.02
$d_{xy}$	0.32	0.35	0.03	0.45	0.50	0.05

orbitals in  $\text{PFe}({}^3E_g/{}^3A_{2g})\cdots\text{CO}$  adducts, while they are significant in the  $\text{PFe}({}^1A_{1g})\cdots\text{CO}$  adduct. In particular, the population of the formally empty  $d_z^2$  orbital of the singlet state increases significantly upon CO binding. At the same time, the population of the formally doubly occupied  $d_{xz}$  and  $d_{yz}$  orbitals decreases. On the basis of these findings, it is clear that the  $\text{Fe}(\text{II})\cdots\text{CO}$  interaction in the singlet state can be understood in terms of the well-known Dewar–Chatt–Duncanson

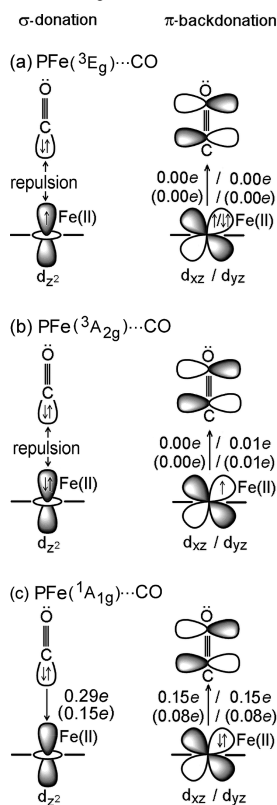
(DCD) bonding model, which was originally introduced to discuss the binding of olefins to transition metals.<sup>123</sup>

A significant  $\sigma$ -donation of charge takes place from the lone pair located on the CO ligand to the empty  $d_z^2$  orbital located on the Fe(II) of the singlet adduct, while at the same time  $\pi$ -backdonation occurs from the  $d_{xz}$  and  $d_{yz}$  orbitals to the empty  $\pi^*$  orbitals of CO, consistent with natural bond orbital (NBO)<sup>124</sup> results (see Scheme S1) and the elongation of the C–O bond length<sup>125</sup> in the PFe(<sup>1</sup>A<sub>1g</sub>)...CO adduct (1.141 Å) with respect to that of free CO (1.125 Å, which is the same as in the PFe(<sup>3</sup>E<sub>g</sub>/<sup>3</sup>A<sub>2g</sub>)...CO complexes). The importance of  $\pi$ -backdonation has been already pointed out on related compounds based on vibrational spectroscopy measurements and DFT computations.<sup>126–128</sup> A schematic representation of the binding modes just discussed, along with the associated amount of the electron transfer ( $\Delta q$ ) based on the Mulliken population analysis, is reported in Scheme 2. Note that electron correlation significantly affects the magnitude of the DCD components, consistent with our previous findings on agostic complexes.<sup>41</sup>

## 5. CONCLUSIONS

The LED analysis in the DLPNO-CCSD(T) framework decomposes the interaction energy of an arbitrary number of fragments of a closed-shell molecular adduct into repulsive electronic preparation and interfragment electrostatic, exchange, and London dispersion contributions. In this study,

**Scheme 2. Schematic Diagram of the  $\sigma$ -Donation and  $\pi$ -Backdonation Taking Place upon CO Binding to the (a) <sup>3</sup>E<sub>g</sub>, (b) <sup>3</sup>A<sub>2g</sub>, and (c) <sup>1</sup>A<sub>1g</sub> States of PFe<sup>a</sup>**



<sup>a</sup>The corresponding amount of electron transfer ( $\Delta q$ ) based on Mulliken population analysis at the DLPNO-CCSD/NormalPNO/def2-TZVP and HF (in parentheses) levels is also reported.

we presented an extension of the LED scheme to open-shell molecular systems that was implemented in the ORCA program package. As a first illustrative case study this scheme was applied to investigate the mechanism that governs the change in the singlet–triplet energy gap of CH<sub>2</sub> upon interaction with water and rare gases (Rg) and of heme (PFe) upon interaction with CO.

The CH<sub>2</sub>...X interaction (X = H<sub>2</sub>O, He, Ne, Ar, and Kr) was found to be attractive for both the triplet <sup>3</sup>CH<sub>2</sub> and the singlet <sup>1</sup>CH<sub>2</sub> methylene. The interaction is stronger with <sup>1</sup>CH<sub>2</sub> than with <sup>3</sup>CH<sub>2</sub>, resulting in a lowering of the singlet–triplet energy gap ( $E_{S-T}$ ). The LED analysis of the CH<sub>2</sub>...H<sub>2</sub>O interaction showed that electrostatics dominates the interaction for both spin states of methylene. The lowering of  $E_{S-T}$  can thus be understood in terms of the larger electrostatic interaction in <sup>1</sup>CH<sub>2</sub>...H<sub>2</sub>O than that in <sup>3</sup>CH<sub>2</sub>...H<sub>2</sub>O, consistent with chemical intuition. In contrast, the interaction of methylene with rare gases (Rg) is dominated by London dispersion forces for both spin states. In this case, the lowering of  $E_{S-T}$  arises from the stronger London dispersion in <sup>1</sup>CH<sub>2</sub>...Rg than that in <sup>3</sup>CH<sub>2</sub>...Rg. This is consistent with the larger polarizability of <sup>1</sup>CH<sub>2</sub> than that of <sup>3</sup>CH<sub>2</sub>.

As regards heme systems, it was found that the PFe...CO interaction is dominated by the correlation contribution for all the spin states of PFe investigated in this work (<sup>1</sup>A<sub>1g</sub>, <sup>3</sup>E<sub>g</sub>, and <sup>3</sup>A<sub>2g</sub>). Although PFe is a triplet in its ground state, the PFe(<sup>1</sup>A<sub>1g</sub>)...CO interaction is significantly stronger than the interaction of PFe in the two lowest-lying triplets (<sup>3</sup>E<sub>g</sub> and <sup>3</sup>A<sub>2g</sub>) with CO, leading to a lowering of  $E_{S-T}$  in the adduct. In fact, the LED analysis demonstrated that PFe(<sup>3</sup>E<sub>g</sub>)...CO and the PFe(<sup>3</sup>A<sub>2g</sub>)...CO adducts can be described as van der Waals complexes stabilized by weak dispersion forces. In contrast, the PFe(<sup>1</sup>A<sub>1g</sub>)...CO bond can be described as a strong donor/acceptor interaction in which electron density is transferred from the carbon lone pair into the formally empty  $d_z^2$  orbital on the central iron atom (Fe(II) ← CO  $\sigma$ -donation) and from the filled  $d_{xz}$  and  $d_{yz}$  orbitals into the  $\pi^*$  antibonding orbitals on the CO molecule (Fe(II) → CO  $\pi$ -backdonation).

It should be stressed here again that the results just discussed refer to the minimal porphyrin model in the gas phase. The presence of heme side chains, solvent, or protein matrices may drastically change the nature of the Fe...CO interaction, especially for triplet heme adducts. However, the tools presented in this work appear to be particularly powerful for the in-depth understanding of intermolecular interactions in adducts with complicated electronic structures, such as heme species.

## ■ ASSOCIATED CONTENT

### 📄 Supporting Information

The Supporting Information is available free of charge on the ACS Publications website at DOI: 10.1021/acs.jctc.8b01145.

Cartesian coordinates and key geometrical parameters of the optimized structures; dependence of the energetics on the computational settings and population analysis; distance dependence of LED terms (PDF)

## ■ AUTHOR INFORMATION

### Corresponding Authors

\*E-mail: frank.neese@kofo.mpg.de.

\*E-mail: giovanni.bistoni@kofo.mpg.de.

ORCID 

Ahmet Altun: 0000-0001-8818-9925

Frank Neese: 0000-0003-4691-0547

Giovanni Bistoni: 0000-0003-4849-1323

## Notes

The authors declare no competing financial interest.

## ACKNOWLEDGMENTS

We gratefully acknowledge the Priority Program “Control of Dispersion Interactions in Molecular Chemistry” (SPP 1807) of the Deutsche Forschungsgemeinschaft for financial support.

## REFERENCES

- (1) Stone, A. *The Theory of Intermolecular Forces*, 2nd ed.; Oxford University Press: Oxford, 2013.
- (2) Hobza, P.; Zahradník, R. *Intermolecular Complexes: The Role of van Der Waals Systems in Physical Chemistry and in the Biodisciplines*; Elsevier: Amsterdam, 1988.
- (3) Wagner, J. P.; Schreiner, P. R. London Dispersion in Molecular Chemistry—Reconsidering Steric Effects. *Angew. Chem., Int. Ed.* **2015**, *54*, 12274–12296.
- (4) Johnson, E. R.; Keinan, S.; Mori-Sánchez, P.; Contreras-García, J.; Cohen, A. J.; Yang, W. Revealing Noncovalent Interactions. *J. Am. Chem. Soc.* **2010**, *132*, 6498–6506.
- (5) Knowles, R. R.; Jacobsen, E. N. Attractive Noncovalent Interactions in Asymmetric Catalysis: Links between Enzymes and Small Molecule Catalysts. *Proc. Natl. Acad. Sci. U. S. A.* **2010**, *107*, 20678–20685.
- (6) Neese, F.; Atanasov, M.; Bistoni, G.; Maganas, D.; Ye, S. Chemistry and Quantum Mechanics in 2019 – Give Us Insight and Numbers. *J. Am. Chem. Soc.* **2019**, DOI: 10.1021/jacs.8b13313.
- (7) Jeziorski, B.; Moszynski, R.; Szalewicz, K. Perturbation Theory Approach to Intermolecular Potential Energy Surfaces of van Der Waals Complexes. *Chem. Rev.* **1994**, *94*, 1887–1930.
- (8) Hohenstein, E. G.; Sherrill, C. D. Wavefunction Methods for Noncovalent Interactions. *Wiley Interdiscip. Rev. Comput. Mol. Sci.* **2012**, *2*, 304–326.
- (9) Morokuma, K. Molecular Orbital Studies of Hydrogen Bonds. III. C=O...H–O Hydrogen Bond in H<sub>2</sub>CO...H<sub>2</sub>O and H<sub>2</sub>CO...2H<sub>2</sub>O. *J. Chem. Phys.* **1971**, *55*, 1236–1244.
- (10) Kitaura, K.; Morokuma, K. A New Energy Decomposition Scheme for Molecular Interactions within the Hartree-Fock Approximation. *Int. J. Quantum Chem.* **1976**, *10*, 325–340.
- (11) Morokuma, K. Why Do Molecules Interact? The Origin of Electron Donor-Acceptor Complexes, Hydrogen Bonding and Proton Affinity. *Acc. Chem. Res.* **1977**, *10*, 294–300.
- (12) Umeyama, H.; Morokuma, K. The Origin of Hydrogen Bonding. An Energy Decomposition Study. *J. Am. Chem. Soc.* **1977**, *99*, 1316–1332.
- (13) Mao, Y.; Horn, P. R.; Head-Gordon, M. Energy Decomposition Analysis in an Adiabatic Picture. *Phys. Chem. Chem. Phys.* **2017**, *19*, 5944–5958.
- (14) Mo, Y.; Gao, J.; Peyerimhoff, S. D. Energy Decomposition Analysis of Intermolecular Interactions Using a Block-Localized Wave Function Approach. *J. Chem. Phys.* **2000**, *112*, 5530–5538.
- (15) Grimme, S.; Hansen, A.; Brandenburg, J. G.; Bannwarth, C. Dispersion-Corrected Mean-Field Electronic Structure Methods. *Chem. Rev.* **2016**, *116*, 5105–5154.
- (16) Grimme, S.; Antony, J.; Ehrlich, S.; Krieg, H. A Consistent and Accurate *Ab Initio* Parametrization of Density Functional Dispersion Correction (DFT-D) for the 94 Elements H–Pu. *J. Chem. Phys.* **2010**, *132*, 154104.
- (17) Caldeweyher, E.; Bannwarth, C.; Grimme, S. Extension of the D3 Dispersion Coefficient Model. *J. Chem. Phys.* **2017**, *147*, 034112.
- (18) Zhao, Y.; Truhlar, D. G. Benchmark Databases for Nonbonded Interactions and Their Use To Test Density Functional Theory. *J. Chem. Theory Comput.* **2005**, *1*, 415–432.

(19) Wang, Y.; Jin, X.; Yu, H. S.; Truhlar, D. G.; He, X. Revised M06-L Functional for Improved Accuracy on Chemical Reaction Barrier Heights, Noncovalent Interactions, and Solid-State Physics. *Proc. Natl. Acad. Sci. U. S. A.* **2017**, *114*, 8487–8492.

(20) Řezáč, J.; Hobza, P. Describing Noncovalent Interactions beyond the Common Approximations: How Accurate Is the “Gold Standard,” CCSD(T) at the Complete Basis Set Limit? *J. Chem. Theory Comput.* **2013**, *9*, 2151–2155.

(21) Řezáč, J.; Hobza, P. *Ab Initio* Quantum Mechanical Description of Noncovalent Interactions at Its Limits: Approaching the Experimental Dissociation Energy of the HF Dimer. *J. Chem. Theory Comput.* **2014**, *10*, 3066–3073.

(22) Řezáč, J.; Hobza, P. Extrapolation and Scaling of the DFT-SAPT Interaction Energies toward the Basis Set Limit. *J. Chem. Theory Comput.* **2011**, *7*, 685–689.

(23) Takatani, T.; Hohenstein, E. G.; Malagoli, M.; Marshall, M. S.; Sherrill, C. D. Basis Set Consistent Revision of the S22 Test Set of Noncovalent Interaction Energies. *J. Chem. Phys.* **2010**, *132*, 144104.

(24) Ramabhadran, R. O.; Raghavachari, K. Extrapolation to the Gold-Standard in Quantum Chemistry: Computationally Efficient and Accurate CCSD(T) Energies for Large Molecules Using an Automated Thermochemical Hierarchy. *J. Chem. Theory Comput.* **2013**, *9*, 3986–3994.

(25) Neese, F.; Hansen, A.; Liakos, D. G. Efficient and Accurate Approximations to the Local Coupled Cluster Singles Doubles Method Using a Truncated Pair Natural Orbital Basis. *J. Chem. Phys.* **2009**, *131*, 064103.

(26) Neese, F.; Hansen, A.; Wennmohs, F.; Grimme, S. Accurate Theoretical Chemistry with Coupled Pair Models. *Acc. Chem. Res.* **2009**, *42*, 641–648.

(27) Neese, F.; Wennmohs, F.; Hansen, A. Efficient and Accurate Local Approximations to Coupled-Electron Pair Approaches: An Attempt to Revive the Pair Natural Orbital Method. *J. Chem. Phys.* **2009**, *130*, 114108.

(28) Hansen, A.; Liakos, D. G.; Neese, F. Efficient and Accurate Local Single Reference Correlation Methods for High-Spin Open-Shell Molecules Using Pair Natural Orbitals. *J. Chem. Phys.* **2011**, *135*, 214102.

(29) Huntington, L. M. J.; Hansen, A.; Neese, F.; Nooijen, M. Accurate Thermochemistry from a Parameterized Coupled-Cluster Singles and Doubles Model and a Local Pair Natural Orbital Based Implementation for Applications to Larger Systems. *J. Chem. Phys.* **2012**, *136*, 064101.

(30) Riplinger, C.; Neese, F. An Efficient and near Linear Scaling Pair Natural Orbital Based Local Coupled Cluster Method. *J. Chem. Phys.* **2013**, *138*, 034106.

(31) Riplinger, C.; Sandhoefer, B.; Hansen, A.; Neese, F. Natural Triple Excitations in Local Coupled Cluster Calculations with Pair Natural Orbitals. *J. Chem. Phys.* **2013**, *139*, 134101.

(32) Liakos, D. G.; Hansen, A.; Neese, F. Weak Molecular Interactions Studied with Parallel Implementations of the Local Pair Natural Orbital Coupled Pair and Coupled Cluster Methods. *J. Chem. Theory Comput.* **2011**, *7*, 76–87.

(33) Riplinger, C.; Pinski, P.; Becker, U.; Valeev, E. F.; Neese, F. Sparse maps—A Systematic Infrastructure for Reduced-Scaling Electronic Structure Methods. II. Linear Scaling Domain Based Pair Natural Orbital Coupled Cluster Theory. *J. Chem. Phys.* **2016**, *144*, 024109.

(34) Liakos, D. G.; Sparta, M.; Kesharwani, M. K.; Martin, J. M. L.; Neese, F. Exploring the Accuracy Limits of Local Pair Natural Orbital Coupled-Cluster Theory. *J. Chem. Theory Comput.* **2015**, *11*, 1525–1539.

(35) Liakos, D. G.; Neese, F. Is It Possible To Obtain Coupled Cluster Quality Energies at near Density Functional Theory Cost? Domain-Based Local Pair Natural Orbital Coupled Cluster vs Modern Density Functional Theory. *J. Chem. Theory Comput.* **2015**, *11*, 4054–4063.

(36) Paulechka, E.; Kazakov, A. Efficient DLPNO-CCSD(T)-Based Estimation of Formation Enthalpies for C-, H-, O-, and N-Containing

Closed-Shell Compounds Validated Against Critically Evaluated Experimental Data. *J. Phys. Chem. A* **2017**, *121*, 4379–4387.

(37) Koerstz, M.; Elm, J.; Mikkelsen, K. V. Benchmark Study of the Structural and Thermochemical Properties of a Dihydroazulene/Vinylheptafulvene Photoswitch. *J. Phys. Chem. A* **2017**, *121*, 3148–3154.

(38) Schneider, W. B.; Bistoni, G.; Sparta, M.; Saitow, M.; Riplinger, C.; Auer, A. A.; Neese, F. Decomposition of Intermolecular Interaction Energies within the Local Pair Natural Orbital Coupled Cluster Framework. *J. Chem. Theory Comput.* **2016**, *12*, 4778–4792.

(39) Altun, A.; Neese, F.; Bistoni, G. Local Energy Decomposition Analysis of Hydrogen-Bonded Dimers within a Domain-Based Pair Natural Orbital Coupled Cluster Study. *Beilstein J. Org. Chem.* **2018**, *14*, 919–929.

(40) Bistoni, G.; Auer, A. A.; Neese, F. Understanding the Role of Dispersion in Frustrated Lewis Pairs and Classical Lewis Adducts: A Domain-Based Local Pair Natural Orbital Coupled Cluster Study. *Chem. - Eur. J.* **2017**, *23*, 865–873.

(41) Lu, Q.; Neese, F.; Bistoni, G. Formation of Agostic Structures Driven by London Dispersion. *Angew. Chem., Int. Ed.* **2018**, *57*, 4760–4764.

(42) Ho, L. P.; Nasr, A.; Jones, P. G.; Altun, A.; Neese, F.; Bistoni, G.; Tamm, M. London Dispersion Interactions in Pnictogen Cations  $[ECl_2]^+$  and  $[E=E]^2+$  (E = P, As, Sb) Supported by Anionic N-Heterocyclic Carbenes. *Chem. - Eur. J.* **2018**, *24*, 18922–18932.

(43) Neese, F. The ORCA Program System. *Wiley Interdiscip. Rev. Comput. Mol. Sci.* **2012**, *2*, 73–78.

(44) Neese, F. Software Update: The ORCA Program System, Version 4.0. *Wiley Interdiscip. Rev. Comput. Mol. Sci.* **2018**, *8*, e1327.

(45) Green, M. C.; Fedorov, D. G.; Kitaura, K.; Francisco, J. S.; Slipchenko, L. V. Open-Shell Pair Interaction Energy Decomposition Analysis (PIEDA): Formulation and Application to the Hydrogen Abstraction in Tripeptides. *J. Chem. Phys.* **2013**, *138*, 074111.

(46) Lein, M.; Szabó, A.; Kovács, A.; Frenking, G. Energy Decomposition Analysis of the Chemical Bond in Main Group and Transition Metal Compounds. *Faraday Discuss.* **2003**, *124*, 365–378.

(47) Marjolin, A.; Gourlaouen, C.; Clavaguéra, C.; Dognon, J.-P.; Piquemal, J.-P. Towards Energy Decomposition Analysis for Open and Closed Shell F-Elements Mono Aqua Complexes. *Chem. Phys. Lett.* **2013**, *563*, 25–29.

(48) Horn, P. R.; Sundstrom, E. J.; Baker, T. A.; Head-Gordon, M. Unrestricted Absolutely Localized Molecular Orbitals for Energy Decomposition Analysis: Theory and Applications to Intermolecular Interactions Involving Radicals. *J. Chem. Phys.* **2013**, *138*, 134119.

(49) Hapka, M.; Żuchowski, P. S.; Szcześniak, M. M.; Chalaśiński, G. Symmetry-Adapted Perturbation Theory Based on Unrestricted Kohn-Sham Orbitals for High-Spin Open-Shell van Der Waals Complexes. *J. Chem. Phys.* **2012**, *137*, 164104.

(50) Żuchowski, P. S.; Podeszwa, R.; Moszyński, R.; Jeziorski, B.; Szalewicz, K. Symmetry-Adapted Perturbation Theory Utilizing Density Functional Description of Monomers for High-Spin Open-Shell Complexes. *J. Chem. Phys.* **2008**, *129*, 084101.

(51) Gonthier, J. F.; Sherrill, C. D. Density-Fitted Open-Shell Symmetry-Adapted Perturbation Theory and Application to  $\pi$ -Stacking in Benzene Dimer Cation and Ionized DNA Base Pair Steps. *J. Chem. Phys.* **2016**, *145*, 134106.

(52) Thellamurege, N.; Hirao, H. Water Complexes of Cytochrome P450: Insights from Energy Decomposition Analysis. *Molecules* **2013**, *18*, 6782–6791.

(53) Costa, P.; Lohmiller, T.; Trosien, I.; Savitsky, A.; Lubitz, W.; Fernandez-Oliva, M.; Sanchez-Garcia, E.; Sander, W. Light and Temperature Control of the Spin State of Bis(*p*-Methoxyphenyl)carbene: A Magnetically Bistable Carbene. *J. Am. Chem. Soc.* **2016**, *138*, 1622–1629.

(54) Richter, G.; Mendez-Vega, E.; Sander, W. Singlet Halophenylcarbenes as Strong Hydrogen-Bond Acceptors. *J. Phys. Chem. A* **2016**, *120*, 3524–3532.

(55) Savin, K. A. Reactions Involving Acids and Other Electrophiles. *Writing Reaction Mechanisms in Organic Chemistry*; Elsevier, 2014; pp 161–235.

(56) Böttcher, T.; Rösenthaler, G.-V. Carbene Adducts of Silicon(IV) Chlorides. *Efficient Methods for Preparing Silicon Compounds*; Elsevier, 2016; pp 339–354.

(57) Herrmann, W. A.; Weskamp, T.; Böhm, V. P. W. Metal Complexes of Stable Carbenes. *Adv. Organomet. Chem.* **2001**, *48*, 1–69.

(58) Standard, J. M. Effects of Solvation and Hydrogen Bond Formation on Singlet and Triplet Alkyl or Aryl Carbenes. *J. Phys. Chem. A* **2017**, *121*, 381–393.

(59) Costa, P.; Sander, W. Hydrogen Bonding Switches the Spin State of Diphenylcarbene from Triplet to Singlet. *Angew. Chem., Int. Ed.* **2014**, *53*, 5122–5125.

(60) Costa, P.; Trosien, I.; Fernandez-Oliva, M.; Sanchez-Garcia, E.; Sander, W. The Fluorenyl Cation. *Angew. Chem., Int. Ed.* **2015**, *54*, 2656–2660.

(61) Costa, P.; Fernandez-Oliva, M.; Sanchez-Garcia, E.; Sander, W. The Highly Reactive Benzhydryl Cation Isolated and Stabilized in Water Ice. *J. Am. Chem. Soc.* **2014**, *136*, 15625–15630.

(62) Henkel, S.; Costa, P.; Klute, L.; Sokkar, P.; Fernandez-Oliva, M.; Thiel, W.; Sanchez-Garcia, E.; Sander, W. Switching the Spin State of Diphenylcarbene via Halogen Bonding. *J. Am. Chem. Soc.* **2016**, *138*, 1689–1697.

(63) Ponka, P. Cell Biology of Heme. *Am. J. Med. Sci.* **1999**, *318*, 241–256.

(64) In *Heme Biology: The Secret Life of Heme in Regulating Diverse Biological Processes*; Li, Z., Ed.; World Scientific: Singapore, 2011.

(65) Poulos, T. L. Heme Enzyme Structure and Function. *Chem. Rev.* **2014**, *114*, 3919–3962.

(66) Sher, E. A.; Shalkai, M.; Shalkai, N. Carbon Monoxide Promotes Respiratory Hemoproteins Iron Reduction Using Peroxides as Electron Donors. *PLoS One* **2012**, *7*, e33039.

(67) Silvernail, N. J.; Noll, B. C.; Schulz, C. E.; Scheidt, W. R. Coordination of Diatomic Ligands to Heme: Simply CO. *Inorg. Chem.* **2006**, *45*, 7050–7052.

(68) Kitagawa, T.; Teraoka, J. The Resonance Raman Spectra of Intermediate-Spin Ferrous Porphyrin. *Chem. Phys. Lett.* **1979**, *63*, 443–446.

(69) Goff, H.; La Mar, G. N.; Reed, C. A. Nuclear Magnetic Resonance Investigation of Magnetic and Electronic Properties of “Intermediate Spin” Ferrous Porphyrin Complexes. *J. Am. Chem. Soc.* **1977**, *99*, 3641–3646.

(70) Collman, J. P.; Hoard, J. L.; Kim, N.; Lang, G.; Reed, C. A. Synthesis, Stereochemistry, and Structure-Related Properties of  $\alpha,\beta,\gamma,\delta$ -Tetraphenylporphyrinatoiron(II). *J. Am. Chem. Soc.* **1975**, *97*, 2676–2681.

(71) Kepp, K. P. Consistent Descriptions of Metal–ligand Bonds and Spin-Crossover in Inorganic Chemistry. *Coord. Chem. Rev.* **2013**, *257*, 196–209.

(72) Walker, F. A.; Simonis, U. Iron Porphyrin Chemistry. *Encyclopedia of Inorganic Chemistry*; John Wiley & Sons, Ltd.: Chichester, UK, 2006.

(73) Saitow, M.; Becker, U.; Riplinger, C.; Valeev, E. F.; Neese, F. A New near-Linear Scaling, Efficient and Accurate, Open-Shell Domain-Based Local Pair Natural Orbital Coupled Cluster Singles and Doubles Theory. *J. Chem. Phys.* **2017**, *146*, 164105.

(74) Guo, Y.; Riplinger, C.; Becker, U.; Liakos, D. G.; Mimenkov, Y.; Cavallo, L.; Neese, F. An Improved Linear Scaling Perturbative Triples Correction for the Domain Based Local Pair-Natural Orbital Coupled Cluster Singles and Doubles Coupled Cluster Method [DLPNO-CCSD(T)]. *J. Chem. Phys.* **2018**, *148*, 011101.

(75) Neese, F. Importance of Direct Spin–Spin Coupling and Spin-Flip Excitations for the Zero-Field Splittings of Transition Metal Complexes: A Case Study. *J. Am. Chem. Soc.* **2006**, *128*, 10213–10222.

(76) Altun, A.; Neese, F.; Bistoni, G. Effect of Electron Correlation on Intermolecular Interactions: A Pair Natural Orbitals Coupled

Cluster Based Local Energy Decomposition Study. *J. Chem. Theory Comput.* **2019**, *15*, 215–228.

(77) Dunning, T. H. Gaussian Basis Sets for Use in Correlated Molecular Calculations. I. The Atoms Boron through Neon and Hydrogen. *J. Chem. Phys.* **1989**, *90*, 1007–1023.

(78) Balabanov, N. B.; Peterson, K. A. Systematically Convergent Basis Sets for Transition Metals. I. All-Electron Correlation Consistent Basis Sets for the 3d Elements Sc–Zn. *J. Chem. Phys.* **2005**, *123*, 064107.

(79) Peterson, K. A.; Dunning, T. H. Accurate Correlation Consistent Basis Sets for Molecular Core–valence Correlation Effects: The Second Row Atoms Al–Ar, and the First Row Atoms B–Ne Revisited. *J. Chem. Phys.* **2002**, *117*, 10548–10560.

(80) Woon, D. E.; Dunning, T. H. Gaussian Basis Sets for Use in Correlated Molecular Calculations. IV. Calculation of Static Electrical Response Properties. *J. Chem. Phys.* **1994**, *100*, 2975–2988.

(81) Weigend, F.; Häser, M.; Patzelt, H.; Ahlrichs, R. RI-MP2: Optimized Auxiliary Basis Sets and Demonstration of Efficiency. *Chem. Phys. Lett.* **1998**, *294*, 143–152.

(82) Eichkorn, K.; Treutler, O.; Öhm, H.; Häser, M.; Ahlrichs, R. Auxiliary Basis Sets to Approximate Coulomb Potentials. *Chem. Phys. Lett.* **1995**, *240*, 283–290.

(83) Becke, A. D. Density-Functional Thermochemistry. III. The Role of Exact Exchange. *J. Chem. Phys.* **1993**, *98*, 5648–5652.

(84) Lee, C.; Yang, W.; Parr, R. G. Development of the Colle-Salvetti Correlation-Energy Formula into a Functional of the Electron Density. *Phys. Rev. B: Condens. Matter Mater. Phys.* **1988**, *37*, 785–789.

(85) Becke, A. D. Density-Functional Exchange-Energy Approximation with Correct Asymptotic Behavior. *Phys. Rev. A: At., Mol., Opt. Phys.* **1988**, *38*, 3098–3100.

(86) Grimme, S.; Ehrlich, S.; Goerigk, L. Effect of the Damping Function in Dispersion Corrected Density Functional Theory. *J. Comput. Chem.* **2011**, *32*, 1456–1465.

(87) Weigend, F. Accurate Coulomb-Fitting Basis Sets for H to Rn. *Phys. Chem. Chem. Phys.* **2006**, *8*, 1057–1065.

(88) Weigend, F.; Ahlrichs, R. Balanced Basis Sets of Split Valence, Triple Zeta Valence and Quadruple Zeta Valence Quality for H to Rn: Design and Assessment of Accuracy. *Phys. Chem. Chem. Phys.* **2005**, *7*, 3297–3305.

(89) Radoń, M.; Pierloot, K. Binding of CO, NO, and O<sub>2</sub> to Heme by Density Functional and Multireference Ab Initio Calculations. *J. Phys. Chem. A* **2008**, *112*, 11824–11832.

(90) Ghosh, A.; Bocian, D. F. Carbonyl Tilting and Bending Potential Energy Surface of Carbon Monoxymes. *J. Phys. Chem.* **1996**, *100*, 6363–6367.

(91) Rovira, C.; Kunc, K.; Hutter, J.; Ballone, P.; Parrinello, M. Equilibrium Geometries and Electronic Structure of Iron–Porphyrin Complexes: A Density Functional Study. *J. Phys. Chem. A* **1997**, *101*, 8914–8925.

(92) Spiro, T. G.; Kozłowski, P. M. Is the CO Adduct of Myoglobin Bent, and Does It Matter? *Acc. Chem. Res.* **2001**, *34*, 137–144.

(93) Bistoni, G.; Riplinger, C.; Minenkov, Y.; Cavallo, L.; Auer, A. A.; Neese, F. Treating Subvalence Correlation Effects in Domain Based Pair Natural Orbital Coupled Cluster Calculations: An Out-of-the-Box Approach. *J. Chem. Theory Comput.* **2017**, *13*, 3220–3227.

(94) Ghafarian Shirazi, R. G.; Neese, F.; Pantazis, D. A. Accurate Spin-State Energetics for Aryl Carbenes. *J. Chem. Theory Comput.* **2018**, *14*, 4733–4746.

(95) Neese, F.; Valeev, E. F. Revisiting the Atomic Natural Orbital Approach for Basis Sets: Robust Systematic Basis Sets for Explicitly Correlated and Conventional Correlated Ab Initio Methods? *J. Chem. Theory Comput.* **2011**, *7*, 33–43.

(96) Bistoni, G.; Polyak, I.; Sparta, M.; Thiel, W.; Neese, F. Toward Accurate QM/MM Reaction Barriers with Large QM Regions Using Domain Based Pair Natural Orbital Coupled Cluster Theory. *J. Chem. Theory Comput.* **2018**, *14*, 3524–3531.

(97) Guo, Y.; Becker, U.; Neese, F. Comparison and Combination of “direct” and Fragment Based Local Correlation Methods: Cluster in

Molecules and Domain Based Local Pair Natural Orbital Perturbation and Coupled Cluster Theories. *J. Chem. Phys.* **2018**, *148*, 124117.

(98) Nakajima, T.; Hirao, K. The Douglas–Kroll–Hess Approach. *Chem. Rev.* **2012**, *112*, 385–402.

(99) Reiher, M. Relativistic Douglas–Kroll–Hess Theory. *Wiley Interdiscip. Rev. Comput. Mol. Sci.* **2012**, *2*, 139–149.

(100) Boys, S. F. Construction of Some Molecular Orbitals to Be Approximately Invariant for Changes from One Molecule to Another. *Rev. Mod. Phys.* **1960**, *32*, 296–299.

(101) Pipek, J.; Mezey, P. G. A Fast Intrinsic Localization Procedure Applicable for Ab Initio and Semiempirical Linear Combination of Atomic Orbital Wave Functions. *J. Chem. Phys.* **1989**, *90*, 4916–4926.

(102) Leopold, D. G.; Murray, K. K.; Miller, A. E. S.; Lineberger, W. C. Methylene: A Study of the  $\bar{X}^3B_1$  and  $\bar{a}^1A_1$  States by Photoelectron Spectroscopy of CH<sub>2</sub> and CD<sub>2</sub>. *J. Chem. Phys.* **1985**, *83*, 4849–4865.

(103) McKellar, A. R. W.; Bunker, P. R.; Sears, T. J.; Evenson, K. M.; Saykally, R. J.; Langhoff, S. R. Far Infrared Laser Magnetic Resonance of Singlet Methylene: Singlet–Triplet Perturbations, Singlet–Triplet Transitions, and the Singlet–Triplet Splitting. *J. Chem. Phys.* **1983**, *79*, 5251–5264.

(104) Apeloig, Y.; Pauncz, R.; Karni, M.; West, R.; Steiner, W.; Chapman, D. Why Is Methylene a Ground State Triplet While Silylene Is a Ground State Singlet? *Organometallics* **2003**, *22*, 3250–3256.

(105) Murray, J. S.; Politzer, P. The Electrostatic Potential: An Overview. *Wiley Interdiscip. Rev. Comput. Mol. Sci.* **2011**, *1*, 153–163.

(106) London, F. The General Theory of Molecular Forces. *Trans. Faraday Soc.* **1937**, *33*, 8b–26.

(107) London, F. Zur Theorie Und Systematik Der Molekularkräfte. *Eur. Phys. J. A* **1930**, *63*, 245–279.

(108) Lallemand, M.; Vidal, D. Variation of the Polarizability of Noble Gases with Density. *J. Chem. Phys.* **1977**, *66*, 4776–4780.

(109) Nir, S.; Adams, S.; Rein, R. On Polarizability Calculations. *Int. J. Quantum Chem.* **1972**, *6*, 295–300.

(110) Zen, A.; Trout, B. L.; Guidoni, L. Properties of Reactive Oxygen Species by Quantum Monte Carlo. *J. Chem. Phys.* **2014**, *141*, 014305.

(111) *CRC Handbook of Chem. and Physics*, 84th ed.; Lide, D. R., Ed.; CRC Press: Boca Raton, FL, 2003.

(112) Willitsch, S.; Imbach, L. L.; Merkt, F. The Ionization Energy of Methylene (CH<sub>2</sub>) from a Rotationally Resolved Photoelectron Spectrum and Its Thermochemical Implications. *J. Chem. Phys.* **2002**, *117*, 1939–1940.

(113) Reiser, G.; Habenicht, W.; Müller-Dethlefs, K.; Schlag, E. W. The Ionization Energy of Nitric Oxide. *Chem. Phys. Lett.* **1988**, *152*, 119–123.

(114) Foner, S. N.; Hudson, R. L. Ionization Potential of the NH Free Radical by Mass Spectrometry: Production of Ground State and Electronically Excited NH by F-Atom Reactions. *J. Chem. Phys.* **1981**, *74*, 5017–5021.

(115) Rohmer, M.-M. Electronic Ground State of iron(II)porphyrin. Ab Initio SCF and CI Calculations and Computed Electron Deformation Densities. *Chem. Phys. Lett.* **1985**, *116*, 44–49.

(116) Obara, S.; Kashiwagi, H. Ab Initio MO Studies of Electronic States and Mössbauer Spectra of High-, Intermediate-, and Low-Spin Fe(II)–Porphyrin Complexes. *J. Chem. Phys.* **1982**, *77*, 3155–3165.

(117) Lang, G.; Spartalian, K.; Reed, C. A.; Collman, J. P. Mössbauer Effect Study of the Magnetic Properties of S = 1 Ferrous Tetrphenylporphyrin. *J. Chem. Phys.* **1978**, *69*, 5424–5427.

(118) Boyd, P. D. W.; Buckingham, D. A.; McMeeking, R. F.; Mitra, S. Paramagnetic Anisotropy, Average Magnetic Susceptibility, and Electronic Structure of Intermediate-Spin S = 1 (5,10,15,20-Tetraphenylporphyrin)Iron(II). *Inorg. Chem.* **1979**, *18*, 3585–3591.

(119) Bikiel, D. E.; Boechi, L.; Capece, L.; Crespo, A.; De Biase, P. M.; Di Lella, S.; González Lebrero, M. C.; Martí, M. A.; Nadra, A. D.; Perissinotti, L. L.; Scherlis, D. A.; Estrin, D. A. Modeling Heme Proteins Using Atomistic Simulations. *Phys. Chem. Chem. Phys.* **2006**, *8*, 5611–5628.



(120) Karpuschkin, T.; Kappes, M. M.; Hampe, O. Binding of O<sub>2</sub> and CO to Metal Porphyrin Anions in the Gas Phase. *Angew. Chem., Int. Ed.* **2013**, *52*, 10374–10377.

(121) Datta, D.; Kossmann, S.; Neese, F. Analytic Energy Derivatives for the Calculation of the First-Order Molecular Properties Using the Domain-Based Local Pair-Natural Orbital Coupled-Cluster Theory. *J. Chem. Phys.* **2016**, *145*, 114101.

(122) Saitow, M.; Neese, F. Accurate Spin-Densities Based on the Domain-Based Local Pair-Natural Orbital Coupled-Cluster Theory. *J. Chem. Phys.* **2018**, *149*, 034104.

(123) Leigh, G. C.; Winterton, N.; Frenking, G. The Dewar-Chatt-Duncanson Bonding Model of Transition Metal-Olefin Complexes Examined by Modern Quantum Chemical Methods. In *Modern Coordination Chemistry*; Winterton, N., Leigh, J., Eds.; Royal Society of Chemistry: Cambridge, 2002; pp 111–122.

(124) Glendenning, E. D.; Landis, C. R.; Weinhold, F. NBO 6.0: Natural Bond Orbital Analysis Program. *J. Comput. Chem.* **2013**, *34*, 1429–1437.

(125) Bistoni, G.; Rampino, S.; Scafuri, N.; Ciancaleoni, G.; Zuccaccia, D.; Belpassi, L.; Tarantelli, F. How P Back-Donation Quantitatively Controls the CO Stretching Response in Classical and Non-Classical Metal Carbonyl Complexes. *Chem. Sci.* **2016**, *7*, 1174–1184.

(126) Vogel, K. M.; Kozłowski, P. M.; Zgierski, M. Z.; Spiro, T. G. Role of the Axial Ligand in Heme-CO Backbonding; DFT Analysis of Vibrational Data. *Inorg. Chim. Acta* **2000**, *297*, 11–17.

(127) Daskalakis, V.; Varotsis, C. Binding and Docking Interactions of NO, CO and O<sub>2</sub> in Heme Proteins as Probed by Density Functional Theory. *Int. J. Mol. Sci.* **2009**, *10*, 4137–4156.

(128) Spiro, T. G.; Soldatova, A. V.; Balakrishnan, G. CO, NO and O<sub>2</sub> as Vibrational Probes of Heme Protein Interactions. *Coord. Chem. Rev.* **2013**, *257*, 511–527.